# APPENDICES
(electronic supplement material)

Sebastiano Foti (Politecnico di Torino, Italy)

Fabrice Hollender (CEA, France)

Flora Garofalo (Politecnico di Torino, Italy)

Dario Albarello (University of Siena, Italy)

Michael Asten, (Monash University, Australia)

Pierre-Yves Bard (ISTerre/IFSTTAR, France)

Cesare Comina (University of Torino, Italy)

Cécile Cornou (ISTerre/IFSTTAR, France)

Brady Cox (Univeristy of Texas at Austin, USA)

Giuseppe Di Giulio, (INGV, Italy)

Thomas Forbriger, (BFO, Germany)

Koichi Hayashi, (Geometrics, USA)

Enrico Lunedei (University of Siena, Italy)

Antony Martin, (Geovision, USA)

Diego Mercerat (CEREMA, France)

Matthias Ohrnberger (Univeristy of Potsdam, Germany)

Valerio Poggi, (SED, ETH, Switzerland)

Florence Renalier (Geophy consult)

Deborah Sicilia (EdF, France)

Valentina Socco (Politecnico di Torino, Italy)

APPENDIX 1.   – CANONICAL CASES (SYNTHETICS)

In this appendix, some canonical V_S profiles and the corresponding Rayleigh wave dispersion curves (fundamental mode and first three overtones) are presented. The following cases are reported:

- Two-layer models with very sharp and sharp velocity contrast (case 1 and 2),

- Shallow (20 m) and deep (40 m) linear velocity gradient models (case 3 and 4),

- Three-layer normally dispersive model with velocity increasing with depth (case 5),

- Three-layer model with velocity inversion in a soft thick and thin 2nd layer (case 6 and 7),

- Three-layer model with velocity inversion in a stiff thick and thin 2nd layer (case 8 and 9).

A constant Poisson's ratio of 0.25 (V_P =1.73 V_S) is assumed for all profiles at all depths. Calculations are carried out using the program *SRFDIS* of Computer Programs in Seismology, vol. IV (Herrmann, 2007).

Case 1: two layers (very high contrast)		

Z (m)	ρ (kg/m3)	V_S (m/s)
0	2000	200
20	2200	800
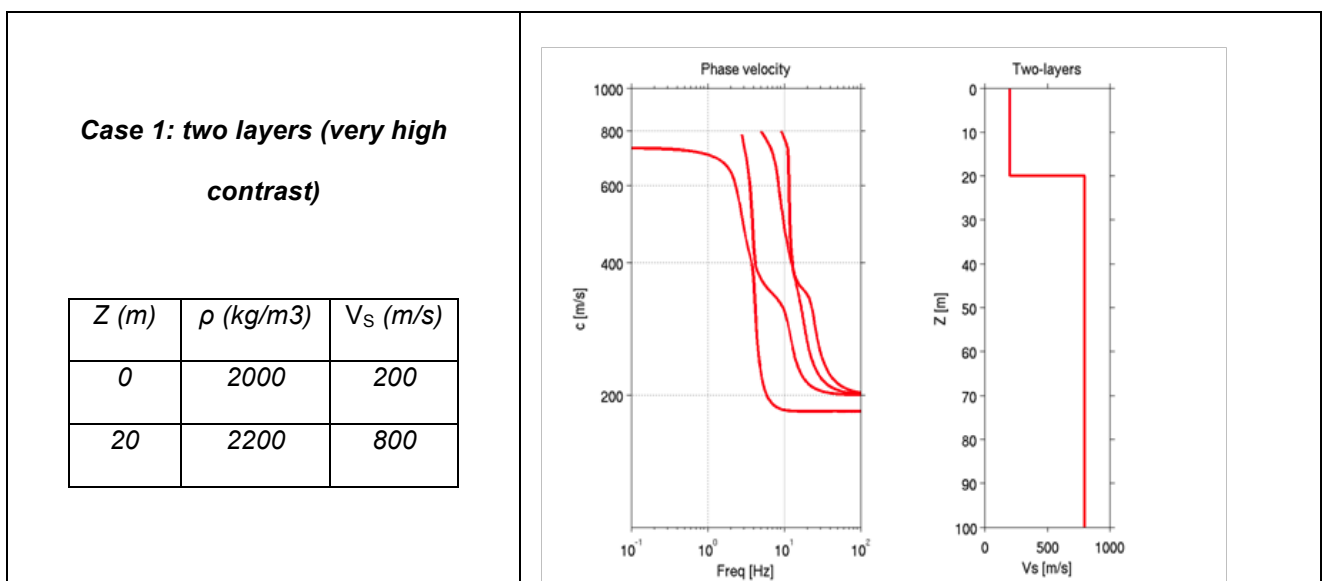
Case 2: two layers (high contrast)

Z (m)	ρ (kg/m3)	V$_S$ (m/s)
0	2000	200
20	2200	600
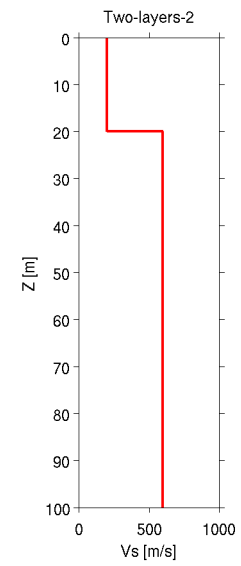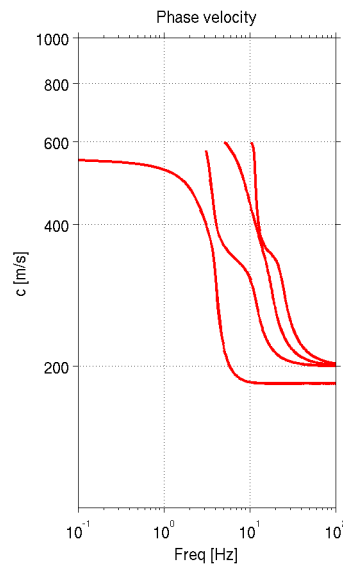
Case 3: velocity gradient model
(shallow)

Z (m)	ρ (kg/m3)	V$_S$ (m/s)
0-20	2000	200+Z*600/20
20	2200	800
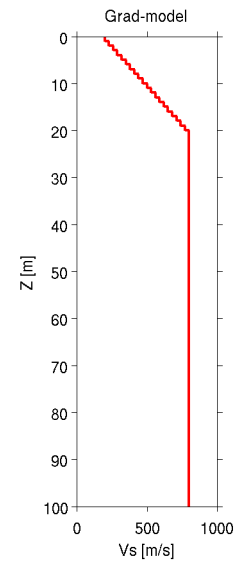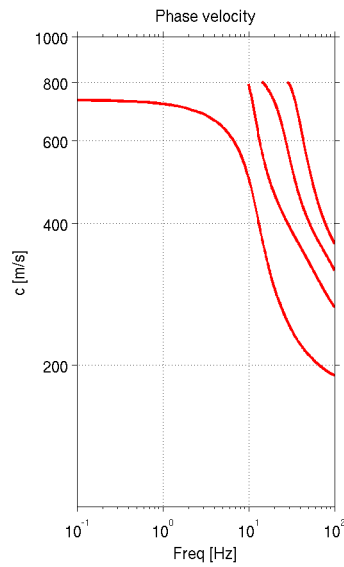
Case 4: velocity gradient model

(deep)

Z (m)	ρ (kg/m3)	V_S (m/s)
0-40	2000	200+Z*600/40
40	2200	800
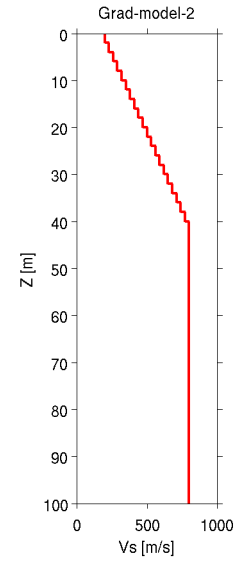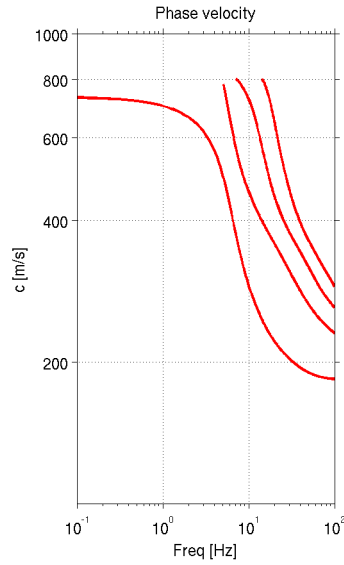
Case 5: three layers (normally

dispersive)

Z (m)	ρ (kg/m3)	V_S (m/s)
0	2000	200
20	2000	500
50	2200	800
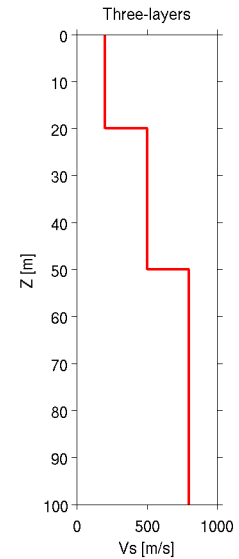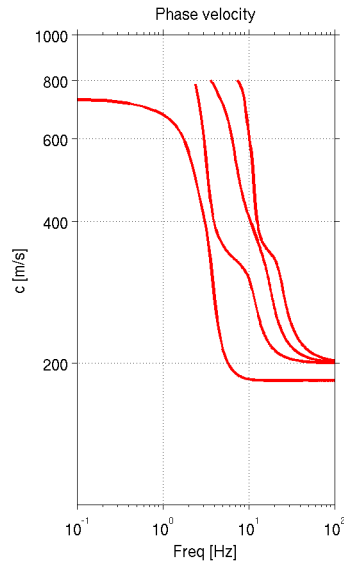
Case 6: three layers (velocity inversion, low-velocity thick layer)

Z (m)	ρ (kg/m3)	V_S (m/s)
0	2000	350
20	2000	250
50	2200	463
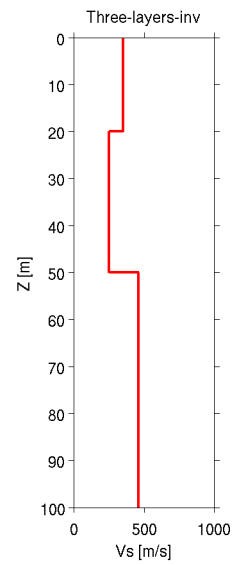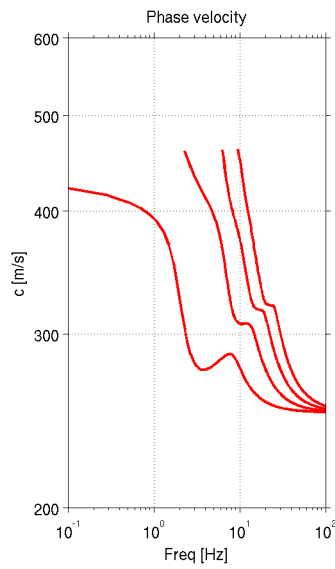
Case 7: three layers (velocity inversion, low-velocity thin layer)

Z (m)	ρ (kg/m3)	V_S (m/s)
0	2000	350
20	2000	250
30	2200	463

Case 8: three layers (velocity inversion, high-velocity thick layer)

Z (m)	ρ (kg/m3)	V_S (m/s)
0	2000	350
20	2000	550
50	2200	463

Case 9: three layers (velocity inversion, high-velocity thin layer)

Z (m)	ρ (kg/m3)	V_S (m/s)
0	2000	350
20	2000	550
30	2200	463
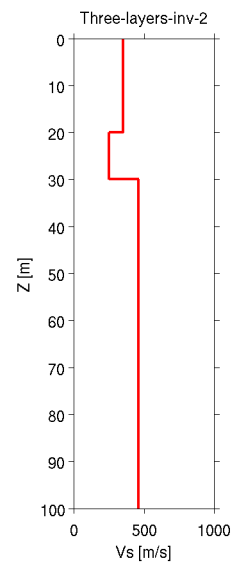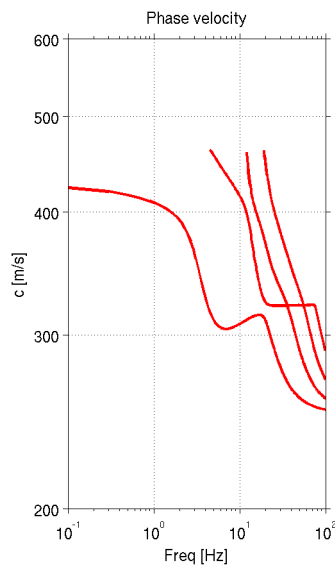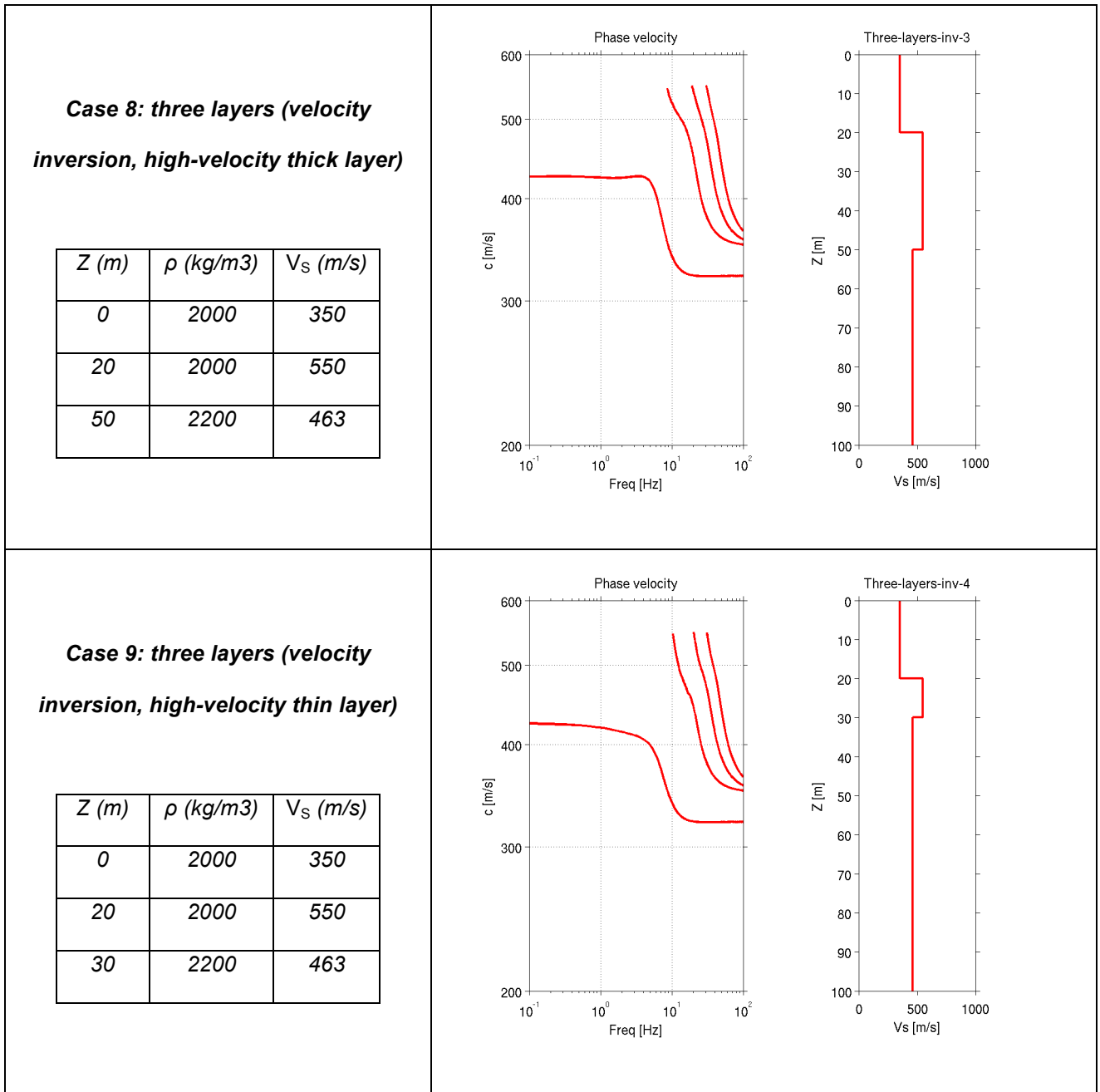
Specific References

Herrmann RB (2007) Computer Programs in Seismology, Version 3.30. St. Louis, MO, Saint Louis University.

APPENDIX 2.   – AMBIENT VIBRATION ARRAY GEOMETRIES

In passive measurements, 2D arrays are preferred to avoid a preferential sampling direction (as in linear arrays, see Appendix 9) since the source position is unknown. The choice of a specific array shape is a compromise between several criteria:

- the number and type of available sensors,

- the available space to install sensors (open space or urban environment),

- the available time to complete the survey on a given site (time to deploy several different arrays in order to enlarge the frequency band of investigation),

- the type of processing (e.g. SPAC or f-k) that will be used to analyse the recorded data,

In this appendix, we present possible geometries as a function of available sensors:

- 4 sensors, which is considered the minimum set,

- 10 sensors, which is a "standard" number of sensors,

- 15/16 sensors.

As already discussed in the main text of the present guidelines, the maximum array aperture should be chosen considering the target investigation depth while the minimum distance between sensors should be chosen considering the minimal desired resolution for the characterization of shallower layers. In order to meet both criteria, it is often necessary to install several arrays with increasing (or decreasing) aperture.

Implementing an array with a set of 4 sensors

When only a few sensors are available, the triangle shape (e.g. 3 sensors on the vertices of an equilateral triangle and 1 sensor in the center) is the best choice. Depending on the target of the survey, several triangles with increasing (or decreasing) apertures can be successively deployed, for example with an increasing (or decreasing) factor of 3 on the size of the triangle. When allowed by the available space, it is better to keep the center sensor at the same location when changing the aperture of the triangle. When space is limited, for example in a town where we have to deal with perpendicular streets, then the placement of sensors can be done as shown in Figure A2.1.

In most cases, with only 4 sensors f-k processing techniques cannot be used; therefore SPAC-like processing techniques are to be used. Depending on the processing algorithm (e.g. standard SPAC), it may be necessary to set up an equilateral triangle with accuracy on sensors location of 5% or better. For other algorithms (e.g. M-SPAC), this issue is less critical.
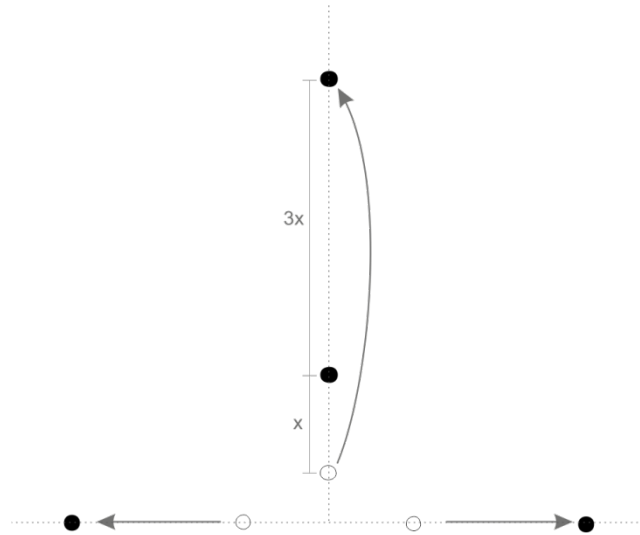
Figure A2.1:   4 sensors triangle in the case of perpendicular crossing roads and sensor shifting between two successive acquisitions with increasing aperture.

Implementing arrays with a set of 10 sensors

Arrays of ten or more sensors are to be preferred for passive array measurements. This allows the use of a wider range of processing approaches (such as f-k) and allows building an array with a better azimuthal coverage and hence a better array response. These advantages improve the chance of retrieving useful dispersion curves (DC) on difficult sites (e.g. rock sites with a low level of ambient vibration).

The most common geometries are:

- circular shape (one sensor in the center and other sensors equally spaced on a circle),

- nested triangles,

- sparse nested triangles,

- T-shape,

- L-shape.

Figure A2.2 shows these geometries with the same number of sensors and the same maximum aperture (with examples of possible distance ratios for L- and T-shape). For circular arrays, the number of sensors on the circle should be an odd number in order to optimize azimuthal coverage.

The theoretical array response for these five geometries is shown in Figures A2.3 and A2.4. The procedure for the construction and interpretation of these array response diagrams is reported in Section 3.1.2 of the main text of these guidelines. In terms of resolution, it is possible to note that the best (lower) k_{min} value (k_{min} being the theoretical minimum wavelength that the array can retrieve if using standard f-k processing) is obtained with the circular array. The two-triangle array presents a slightly higher k_{min} value. The L-shape array shows an overall rather acceptable value, but with a preferential azimuth exhibiting lower array resolution. The T-shape array presents a rather high value of k_{min}, which corresponds to poor array resolution capability. In terms of aliasing the best (higher) value of $k_{max,}$ is obtained with the sparse nested triangle array given that this geometry has the shortest inter-station distance. T-shape arrays may suffer large aliasing even for small wavenumbers for specific source azimuths. L-shape and nested triangle geometries present about the same k_{max} value.

When using SPAC methods the maximum wavelength rule is a much less strict rule. Maximum useable wavelengths are typically a factor 2 to 5 times smaller than those predicted by the k_{min} rule, depending on data quality.

Hence, from a theoretical point of view, for the same number of sensors, the circular array is to be preferred. When the available space is limited (e.g. where access is limited to two perpendicular roads), L-shape or T-shape arrays are acceptable alternatives.

Depending on the requirements of the survey, several arrays with increasing (or decreasing) aperture can be successively deployed. In order get some overlap between the different DC curves that will be retrieved from each array, we recommend using an incremental factor equal or lower than 3 between the apertures of two successive arrays.

As specified above, depending on the processing algorithm (e.g. standard SPAC), it may be necessary to set up arrays with geometry as accurate as possible in terms of interstation distances (accuracy at most 5% of the distance from the array central sensor). For other algorithms (like M-SPAC or f-k), this issue is less critical.

a. Circular shape

b. Nested triangles

c. T-shape

d. L-shape

e. Sparse nested triangle
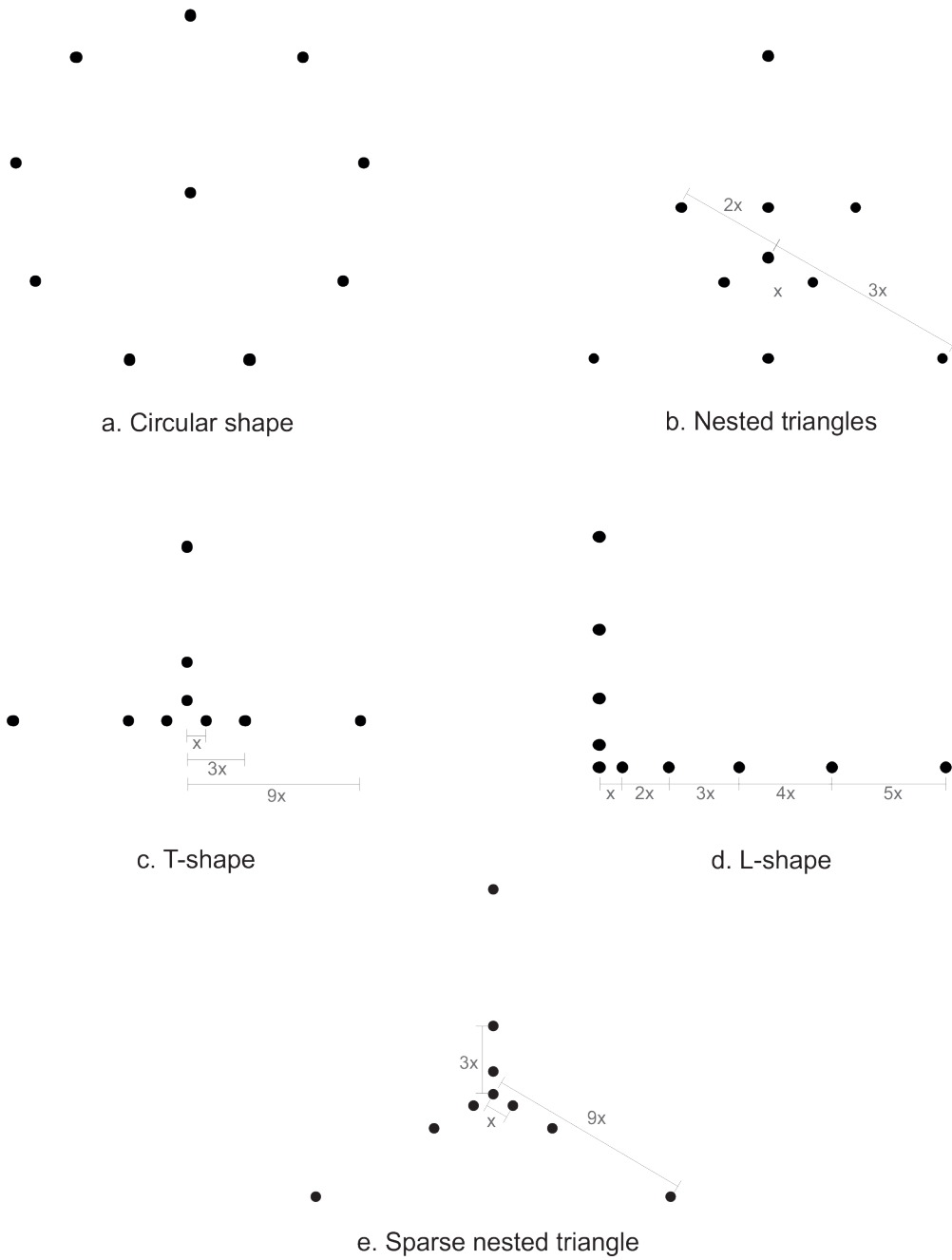
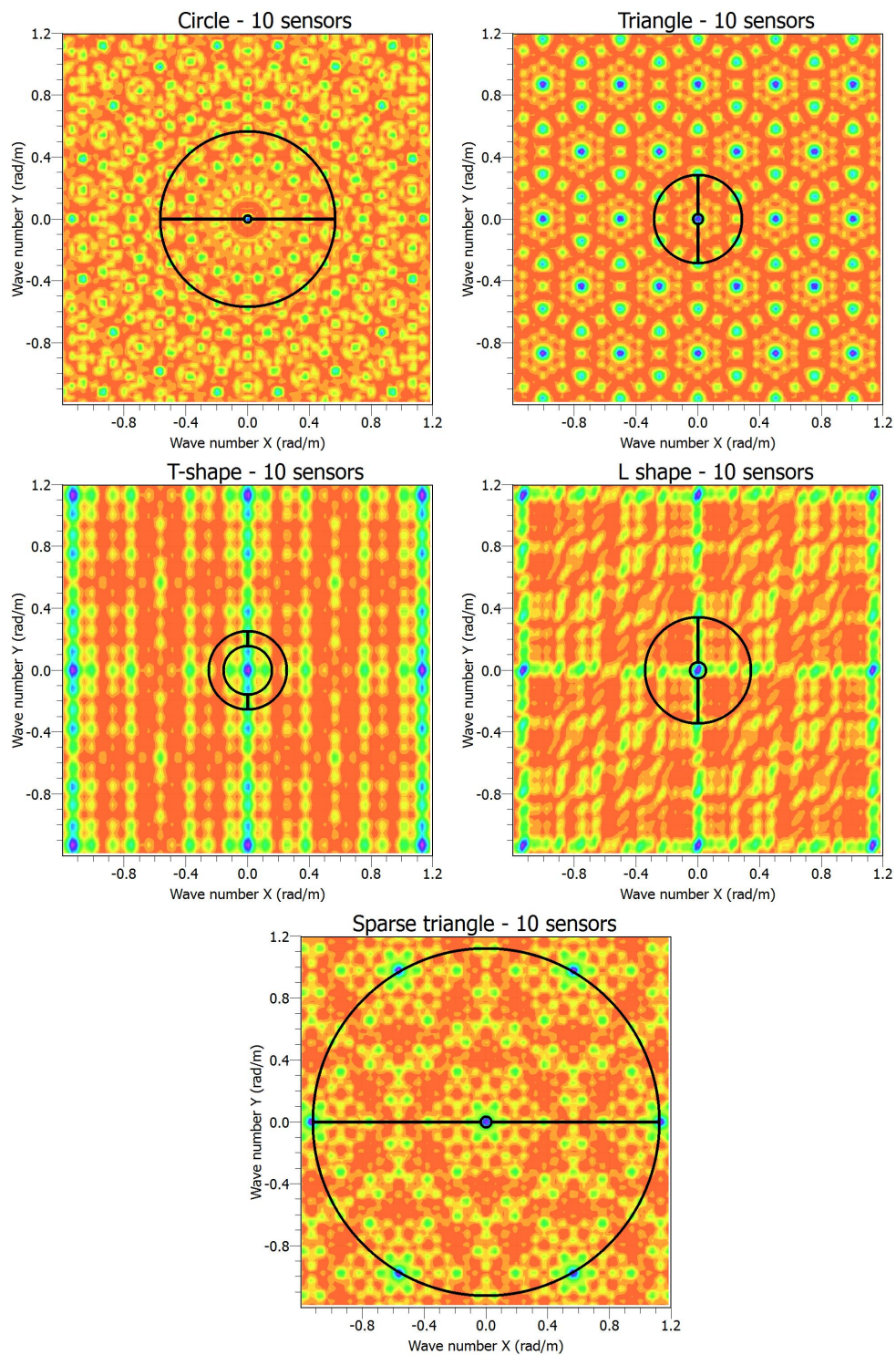*Figure A2.2:   Examples of possible geometries with 10 sensors.*

Figure A2.3:   Array response diagrams for the five geometries presented in Figure A2.2: large scale image for a good representation of k_{max}.
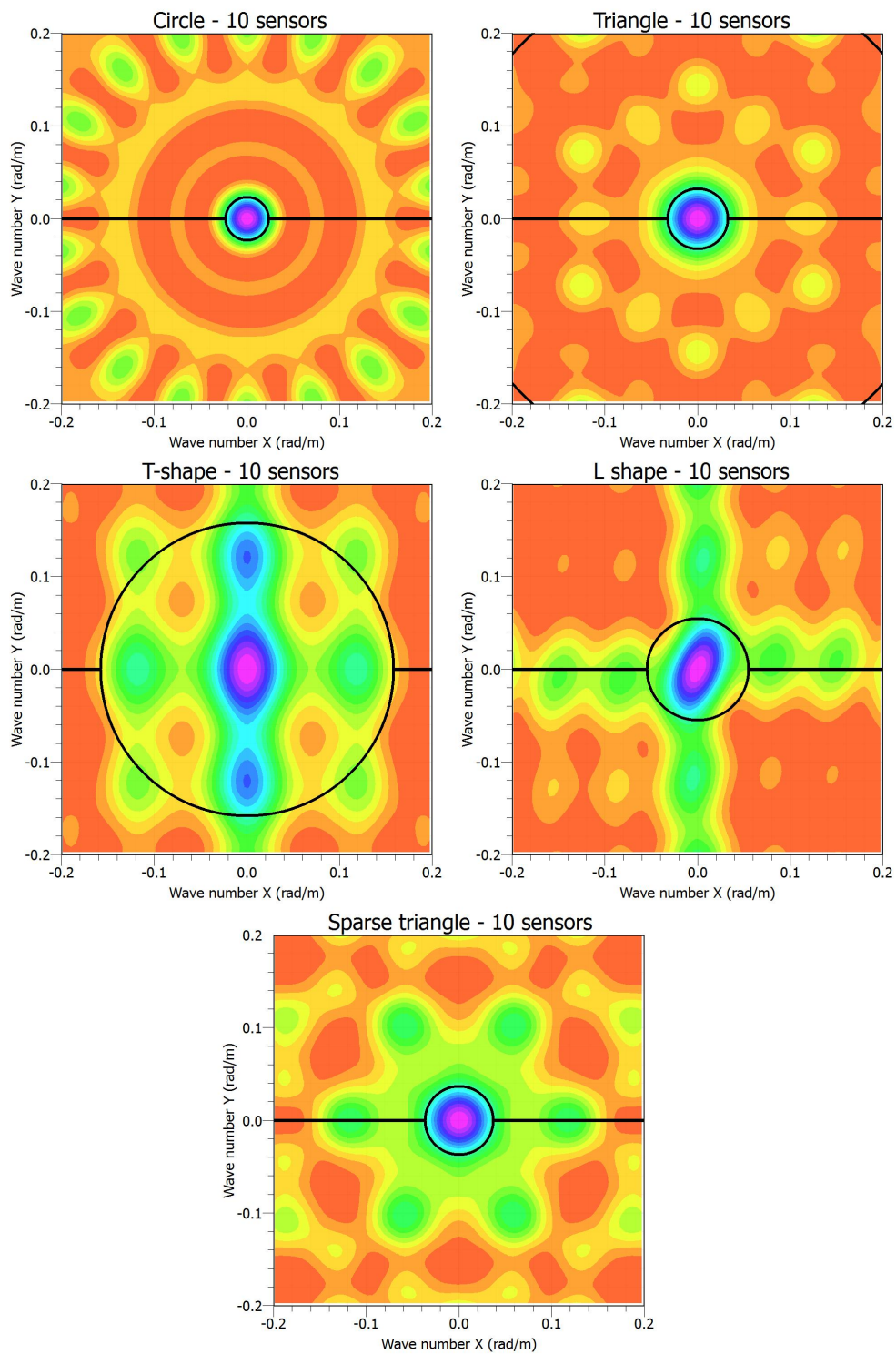
Figure A2.4:   Array response diagrams for the five geometries presented in Figure A2.2: enlargement on the central lobe for a good representation of k_{min}.

Implementing arrays with a set of 15 to 16 sensors

A large number of sensors allows acquiring simultaneously data over different array apertures. For example, it is possible to increase the number of nested triangles or to build two (or more) concentric circles. Figure A2.5 shows possible geometries for a composite circular array with a center sensor (15 sensors) and for a nested-triangle array using 16 sensors. For the double-circle geometry, we recommend the use of a ratio of 3 between the two radii and, in order to optimize azimuthal coverage, to shift the larger circle sensors azimuths with respect to those of the smaller circle. The theoretical array response for these two geometries is given on Figure A2.6. The criterion is a bit favorable (i.e. lower k_{min}) for the double-circle geometry. In terms of the aliasing limit (k_{max}), the two circles provide a very good performance in comparison with the nested-triangles.

Depending on the requirements of the survey, several arrays with increasing (or decreasing) apertures can be successively deployed. In order get a minimal overlap between the different DC curves that will be retrieved from each array, we recommend using an incremental factor equal or lower to 3 between the apertures of two successive arrays. If using the double-circle geometry, we can increase the aperture of the array by moving only the sensors of the inner circle to build the next outer circle, as shown in Figure A2.7. This will lead to a very good overlap between successive acquisitions.

a. Two nested circles
in a composite circular array (15 sensors)

b. Nested triangles (16 sensors)

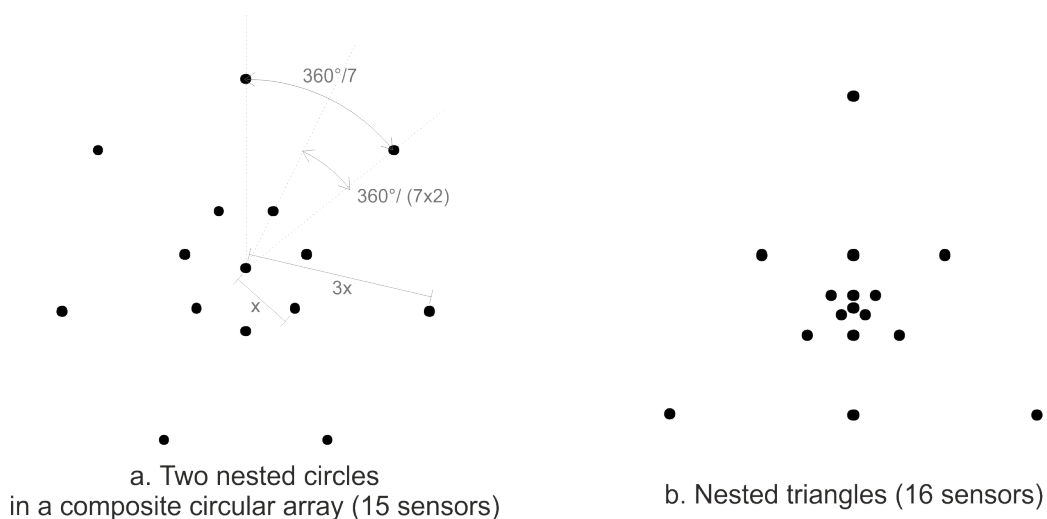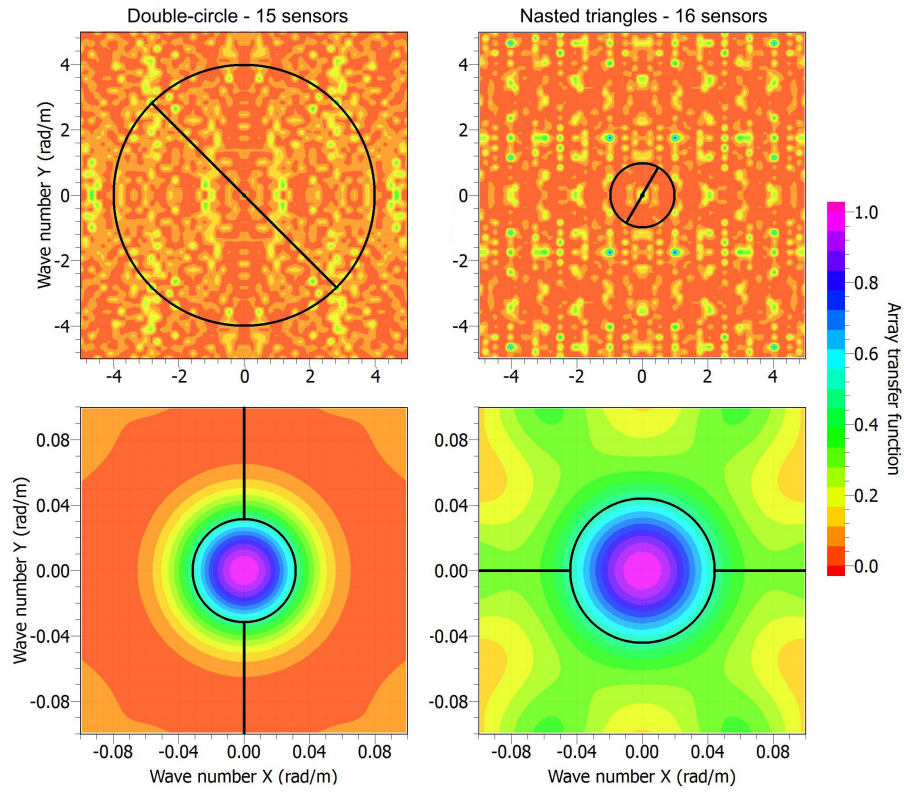*Figure A2.5: Standard geometries with 15 or 16 sensors.*

Figure A2.6: Array response diagrams for the two geometries presented in Figure A2.5. Top: large scale image for a better appreciation of k_{max}; Bottom: zoom on the central lobe for a better appreciation of k_{min}..
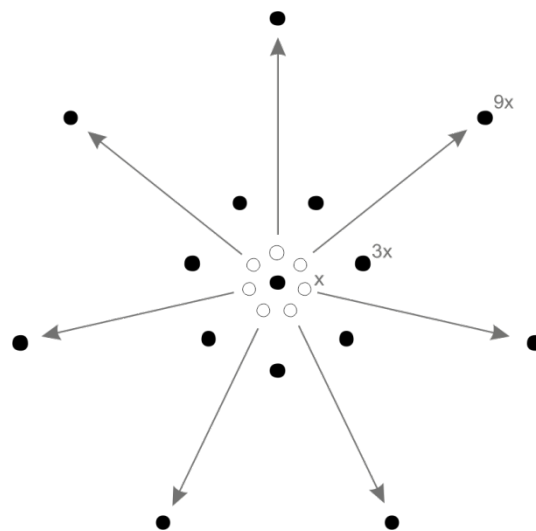

Figure A2.7: 15-sensor double-circle geometry and sensor shifting between two successive acquisitions with increasing aperture.

APPENDIX 3.   – TESTING AND VERIFICATION OF INSTRUMENTATION FOR PASSIVE ARRAYS

While the testing of instruments is relatively easy for "active" measurements, it is more demanding for passive measurements. First of all, it is important to have documentation on instrument characteristics, performance and calibration before attempting field measurements. It is also useful to have information from prior surveys on sites of similar geology and ambient vibration level.

In general, there are no "good" or "bad" sensors. The ability of a given sensor to properly record ambient vibration at a given site depends on several parameters such as: the quality of the sensor installation in the field (see Section 2.2.1 in the main text of these guidelines), the weather conditions (presence of rain of wind), the intrinsic quality of the sensors (e.g. self-noise…), and above all, the level of ambient vibrations (i.e. the desired signals) at the measurement site.

Some sensors may produce good results on a site where ambient vibration signal levels are high, whereas the same sensors, with the same setup, and the same weather conditions, may fail when recording ambient vibrations at a site where ambient vibration levels are very low. So, it is also important to get information on instrument performance at several sites with several different levels of ambient vibrations. Figure 13 in main text of these guidlines shows the high difference in ambient vibrations levels one can get at various sites (examples from the InterPacific project, see Garofalo et al. 2016a and b).

The instrument testing and verification procedures for passive surveys should start before the survey, and be complemented with further tests in the field.

Testing instrumentation before field observations

A good approach for testing instrumentation is to perform "huddle tests" which consist in: setting up all the sensors, with rigorously identical settings, at a single location, as close as possible to each other; record ambient vibrations; compare signal outputs (especially synchronization and phase consistency between the sensors).

In addiction to a standard comparison of records in the time domain, we recommend an analysis of the power spectral density recorded by each sensor and of the frequency-domain coherence function between each pair of sensors. This last analysis is very important since it checks the quality of the signal phase, which is of paramount importance for array processing.

Figure A3.1 shows the results in terms of power spectral density (PSD) and coherency for two huddle tests made with the same set of 6 sensors (in this case, a set of 1s velocimeters) on two very different sites: a high ambient vibration site (Grenoble), and a rather low ambient vibration site (Cadarache). See Garofalo et al. 2016a for more details on these sites.

We first analyze the results in terms of PSD. All sensors produce overall the same spectra on each site (so, there is no reason to identify any sensor as deficient up to this point). Clearly, there is a very high difference in terms of ambient vibration levels between the two sites (up to 40 dB around 2 Hz).
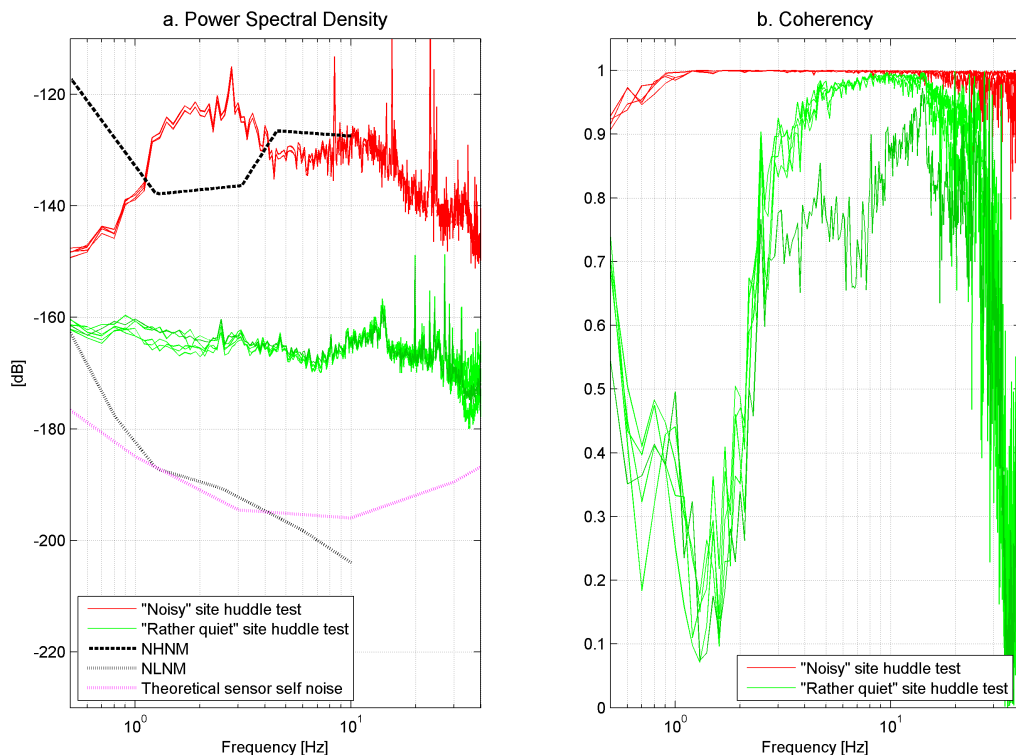
Figure A3.1:   Huddle test results at Cadarache (green) and Grenoble (red) sites. The outlier coherence

function in Cadarache is an example of sensor that has an issue.

On the coherency analysis, the results at the Grenoble site are satisfactory since the coherency is almost equal to one from 1 to 20 Hz. However, at the Cadarache site, the coherency drastically drops for frequencies below 3 Hz, and we can then anticipate poor results in terms of passive array analysis for this frequency band at this site (and likewise at any other site having a similar low level of ambient vibrations in a frequency band of interest). This clearly illustrates the fact that a particular sensor could be suitable for one site, in a given frequency band, but may have severe limitations if used at other sites. Moreover, one can see that one sensor presents a coherency curve that is very different (and lower) than the other ones. This is clearly a faulty sensor that needs repair.
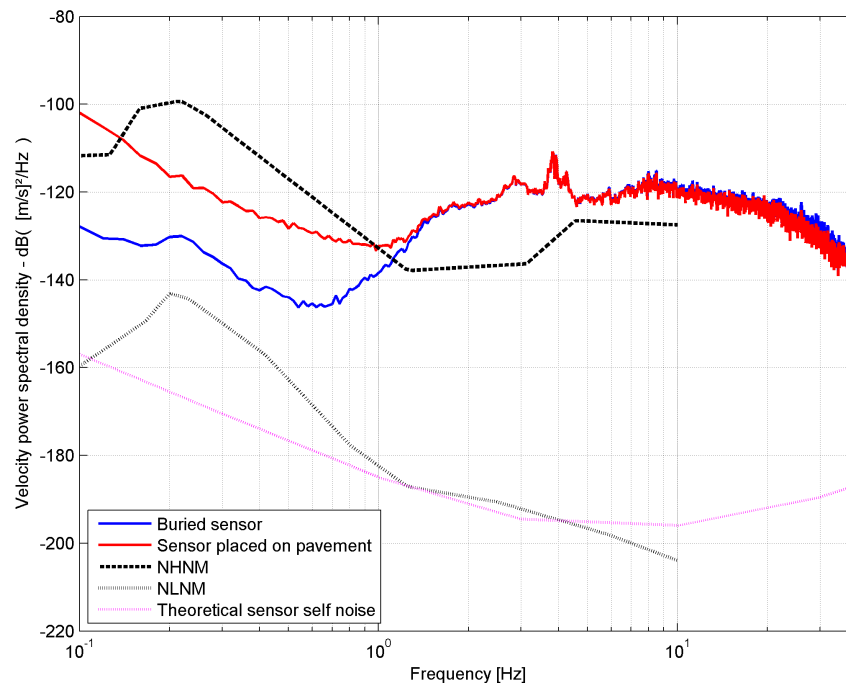
Figure A3.2:   Influence of sensor installation on power spectral density for two identical sensors (30 s seismometers) placed 50 cm apart. The first sensor is firmly half-buried in the soil; the second one is placed on a pavement. Below 1 Hz, the sensor placed on pavement shows noise due to a non-optimal setup and will probably not be suitable for low-frequency analysis (data from Mirandola InterPacific experiment).
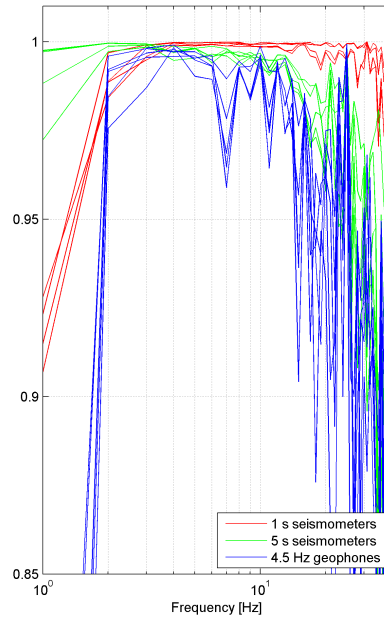
Figure A3.3:   Huddle-test results at Grenoble with different sensors. At this site, the 1 s seismometers

present the best coherency above 3 Hz, whereas the 5 s seismometers are better below 3 Hz.

Huddle tests may be useful:

−   to test the sensor performance under different levels of noise;

−   to test the influence of different acquisition parameters on the quality of the recordings (for

example, if some seismometers have different modes of low-frequency compensation, recording

with different parameterization may help to identify the best one);

−   to test whether a warming up delay is required to achieve stability, in order to get the best

coherency;

−   to test different set-ups and their influence on results (e.g., Figure A3.2 shows the differences in

terms of PSD obtained from a sensor half-buried in the soil, compared with another one just

placed on a pavement);

−   to compare the performance of several different types of sensors (e.g., Figure A3.3 compares

the coherency of three kinds of sensors at the same site);

−   to identify sensors that need a repair.

Verifying instrumentation at field sites

In the field, several successive arrays with different apertures are often deployed. Starting with the smallest array allows analyzing data from a sort of huddle test during the acquisition of the first array. Indeed it is possible to consider a small array as a huddle test, at least up to a given frequency, and verify correct instrument performance. This allows checking (and if possible correct) several performance issues. This stage is therefore obviously preferable before spending time setting up the larger arrays. Having instrumentation that allows real-time data transmission and a software system that displays all signals simultaneously is useful in this context. Wireless transmission of data is therefore an obvious advantage.

With such instrumentation, we can compute, after a few minutes of recording in the field, power spectral densities and coherencies, and perform a trial analysis as previously discussed. This will allow us:

– to identify possible issues with sensors (which can then be exchanged for spare items if a quick repair is not possible),

– to know the overall level of ambient vibration on the site, and hence some information about the chances of getting good results at the site (or, for example, change the installation method used for the sensors) ;

– to check the synchronization of all sensors. Problems with synchronization (which is usually obtained through a GPS system) are quite frequent, but can be easily checked by looking at the time histories after applying a band pass filter (e.g. [1 – 2] Hz, although this frequency band can be adapted at each site depending on the local features of the ambient vibrations). For a small array and at frequencies around 1 Hz, all signals should be almost synchronized. It is easier to perform this test on the vertical component. Figure A3.4 gives an example of this kind of test with one sensor that is not correctly synchronized.
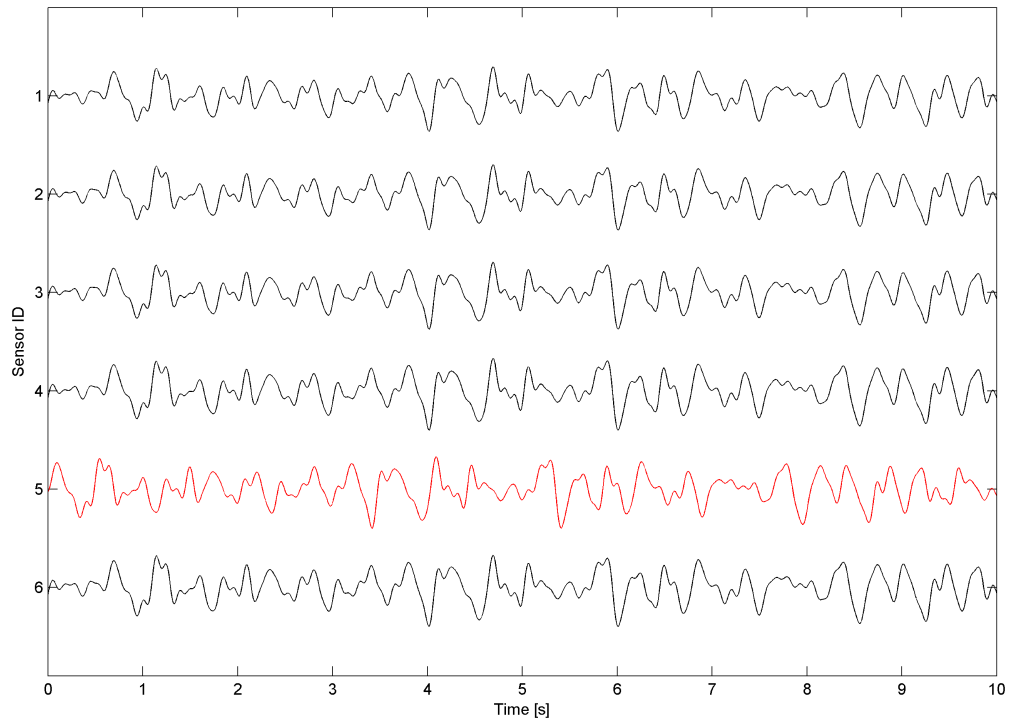
Figure A3.4:   Example of synchronization check. The sensor #5 shows a problem with synchronization; it is in advance of about 0.6 s.

APPENDIX 4.   EXAMPLES OF FIELD SHEETS FOR ACTIVE AND PASSIVE MEASUREMENTS

In this appendix, examples of "field sheets" that the operator may fill during acquisition are proposed. Of course, the best "field sheets" are the ones that are adapted to the operator practices and materials. Therefore, the proposed examples have to be adapted for the specific conditions.

The field sheets that are given here are the ones that were used during the InterPacific project. There are two pages for the MASW acquisition and two pages for one AVA acquisition. For a whole survey at a given site that involves, for example, two different MASW measurement lines and three AVA geometries (e.g. for three increasing aperture cycle arrays), we may need to fill 2 "pairs" of pages for MASW + 3 "pairs" of pages for AVA.

The designations of most boxes in these sheets are self-consistent; just a few comments are given below.

AVA

- Often, the designation of a given sensor (for example: S01 for "sensor number one") is not the same that the designation of a given measuring point (for example R15_A2 for "15 m radius, second azimuth"), that's why there are two distinct columns (Sensor ID and Location ID).
- In the "coupling" column, indicate if a sensor is on a pavement (e.g. "P") or buried ("B") or half-buried ("HB") in the soil.
- "Synchro check" means that the synchronization on the specific sensor (usually achieved by GPS) is OK.
- "Leveling check" means that the leveling of the sensor is OK and no component is clipped due to leveling issues.
- "Signal check" means that the signal has been checked (visual inspection of time series and/or spectra, coherence checking on cross-spectra).

MASW

- One shot series indicates the set of records that corresponds to the same geophones position and polarity with the same shot position and orientation. In other words, all record sets that could be stacked latter. For convenience, they can be labeled as 1, 2, 3, ...

- Type of shot: "V" for vertical shots (and geophones) for Rayleigh experiment, "H1 & H2" for horizontal shots (and geophones) for Love experiment. "H1" means (for example) hitting the beam in one direction, "H2" means hitting the beam in the opposite direction.

- "Hammer person": initials of the person that strikes the hammer (not useful if mechanical sources are used).

- "First filename" / "last filename": depending on the acquisition system, one "individual shot" record is stored in a given file, containing an incremented number. Indicate here first and last recorded files.

Project:	Site:	Date:	*Interpacific ambient vibration array field sheet (1/2)*
Seismological equipment:		**Geomatic equipment:**	
Operators:		**Weather conditions:**	
Array short name:		**Short array description:**	

	GMT	**Local**	**Global environment:**
Begin time:			
End time:			

Array sketch:

Sensor ID	Location ID	Coupling	Synchro check	Levelling check	Signals check	Comment

Site: / *Short array description:* / *Date:* / *Interpacific ambient vibration array field sheet (2/2)*

Sensor ID	Location ID	Coupling	Synchro check	Levelling check	Signals check	Comment

Project:	Site:	Date:	*Interpacific MASW field sheet (1/2)*

MASW equipment:	**Geomatic equipment:**

Operators:	**Weather conditions:**

MASW short name/ID:	**MASW array description:**
Folder name:	

	TU	Local	**Global environment:**
Begin time:			
End time:			

Sampling frequency		**Pre-trigger (s)**	
Gains (high / low)		**Record duration (s)**	
Low pass filter		**Geophone frequency**	
Geophone spacing (m)		**Total length (m)**	

Sensor line sketch (mention if spikes or tripods are used):

Site:			MASW short name/ID:			Date:	*Interpacific MASW field sheet (2/2)*
Shot series	Type of shot (V, H1 or H2)	Hammer person	Shot offset	First filename	Last filename	Comments	

APPENDIX 5.   – DEALING WITH HIGHER MODES IN SURFACE WAVE ANALYSIS

The propagation of seismic waves is a complex phenomenon strongly influenced by the properties of the hosting medium and of the local disturbance that generates the wave. From the mathematical point of view, this can be referred as an initial boundary value problem, which can be resolved as the superposition of normal modes of vibration (Aki and Richards, 1980). Analysis of surface wave is very often performed in terms of modal propagation considering the associated problem of free Rayleigh (or Love) vibrations rather than the complete wavefield generated by the local disturbance (i.e. the seismic source). This simplification may lead to gross errors if modal superposition is not appropriately accounted for (e.g. Tokimatsu, 1987; O'Neill and Matsuoka, 2005; Maraschini et al., 2010).

In principle, the spectral analysis of the experimental wavefield can lead to the proper identification of the free Rayleigh modes if an adequate spatial sampling is available (e.g. Gabriels et al., 1987). Fundamental and higher modes can then be used for the solution of the inverse problem aimed at the estimation of model parameters (e.g. the shear wave velocity profile).

However, the lack of spatial resolution (mainly due to the available number of channels) or complex site response may prevent the possibility of separating the modes of propagation. As a consequence, in complex stratigraphic conditions, only an apparent or effective dispersion curve may be retrieved (Tokimatsu, 1997). Refinements of the signal processing strategies may help in mitigating the lack of spatial resolution, but most severe limitations are associated with the actual spatial sampling of the wavefield, hence they cannot be fully resolved (Foti et al., 2014). Several different strategies have been proposed in the literature to deal with higher modes, but none of them can yet be considered the standard practice. At present, only a limited number of commercial codes for the analysis of surface waves implements an algorithm to fully cope with higher modes influence. A brief outline of some techniques is reported in the following with the associated references.

Simultaneous inversion of multiple modes

The inversion algorithms described in Section 4 can be applied to fundamental and higher modes defining an inverse problem which is in principle better constrained than the inverse problem based on the fundamental mode alone (e.g. Herrmann, 2007; Gabriels et al., 1987). Crucial issues in this respect are related to the full

separation of the modes during signal processing and to the correct identification of the mode number for each branch (Lu and Zhang, 2006). Maraschini et al. (2010) proposed an inversion scheme that defines the misfit function on the determinant of the propagator matrix (e.g., in the Haskell-Thomson formulation) to bypass this limitation. This approach is very convenient for the application to global search methods as it is not computationally intensive (Maraschini and Foti, 2010). An example of application is reported in Figure A5. 1.
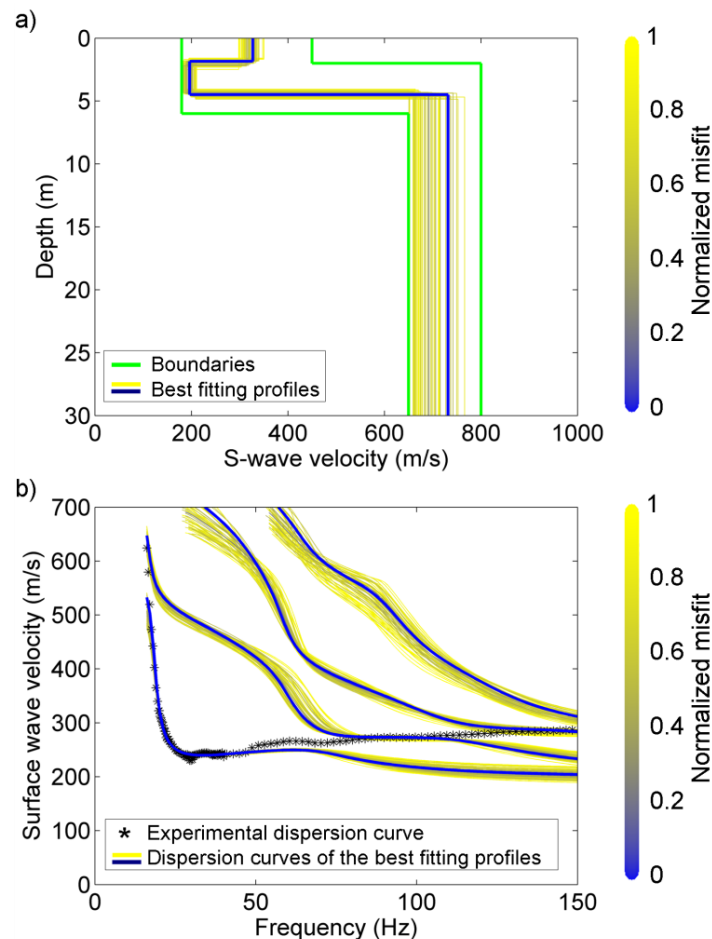

Figure A5. 1– *Example of results obtained with a stochastic multimodal inversion: a) best fitting profiles are reported using a color scale that represents the goodness of fit. The green lines represent the boundaries of the model parameter space; b) the experimental dispersion curve is compared to the theoretical modal dispersion curves associated to each shear wave velocity profile, using the same color scale. Likely because of lack of spatial resolution in the acquisition of surface wave data, an apparent experimental dispersion curve was obtained. The fundamental mode is dominant only over a relatively narrow frequency band (20-50Hz), whereas the propagation is governed by the first higher mode in the low-frequency band and by a progressive shift towards higher modes in the high-frequency band (see also Section **Errore. L'origine riferimento non è stata trovata.** of the main text of these guidelines) (Maraschini and Foti, 2010).*

Inversion of the apparent or "effective mode" dispersion curve

Where very strong velocity contrasts exist at a layer interface, or where a low-velocity layer exists between two higher-velocity layers, as well as in other situations, propagation of Rayleigh-wave energy may occur dominantly in higher modes. Rayleigh-wave modes are typically labelled R_0 (the fundamental mode, which is most common), R_1 (first higher mode), R_2 (second higher mode) etc. The partition of energy among modes is dependent on both the layer velocities (i.e. specific impedance contrasts) and attenuation and on the nature and depth of the wave sources (whether vertical impact or other types of source). If we assume that sources are from vertical impacts, and the subsoil deposit consists of laterally homogeneous layers, then the energy partition between different modes can be theoretically computed (e.g., Ikeda et al, 2012) and we can define an "effective mode", often labelled R_e. Figure A5. 2 shows the first three theoretical Rayleigh-mode phase-velocity dispersion curves for a high-contrast interface at depth 20m, and also shows the dispersion curve for the effective mode. It is clear that for most of the frequency band of interest the R_0 mode dominates, but between 5 and 10 Hz a significant fraction of the Rayleigh wave energy propagates in the R_1 mode, with the result that the R_e dispersion curve shows an upward notch to higher velocities in that frequency band.
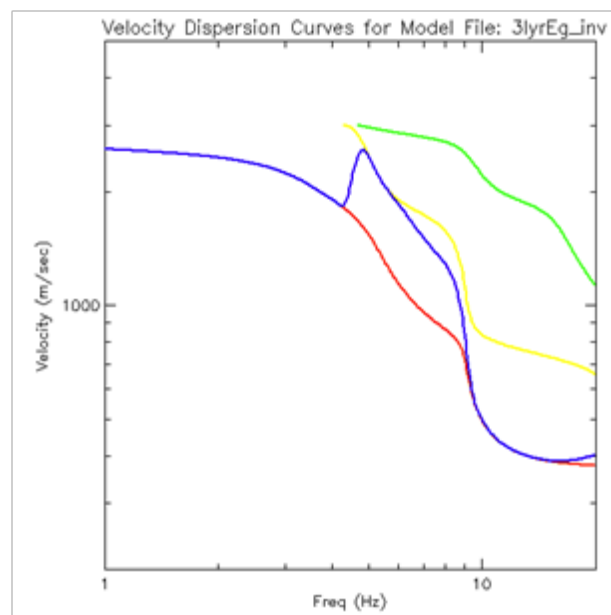

Figure A5. 2 – Example of theoretical dispersion curves for three Rayleigh modes over a high-contrast interface. Red, yellow, green lines show dispersion curves for modes R_0, R_1, R_2. The blue line is the effective mode R_e. The model has 2 layers, V_S=400m/s, thickness 20 m, overlying a hard basement V_S =2000 m/s.

Moreover, an effective dispersion curve can be computed for any kind of source as an equivalent mode, which is able to reproduce the observed coherence (e.g., Lunedei & Albarello, 2009).

The experimental apparent dispersion curve can be the target of the inversion process by using a solution of the forward problem that accounts for mode superposition. For active surface wave methods, this approach was initially proposed for the 2-station SASW method since with its experimental set-up it was not possible to separate the contribution of different modes of propagation (Stokoe et al., 1994). The approach has been successively applied to multi-station approaches (Tokimatsu, 1997). A crucial element to be considered is that the apparent dispersion curve is a function of the source properties and of the experimental configuration (source-to-array distance and inter-receiver spacing), hence a full simulation requires these elements to be explicitly taken into account. Lai et al. (2014) proposed an explicit formulation for the apparent dispersion curve.

For passive surface wave methods (ambient vibration analysis), the nature of the source is unknown, and the inversion of the effective mode is a subject of ongoing study. Indeed the assumptions required for modelling the effective mode may not be sufficient to model an observed effective mode dispersion curve. This limitation is likely to be especially important where lateral inhomogeneities exist and give rise to possible additional conversions of energy between modes.

Inversion of the wavefield transforms

Rather than considering the dispersion curve to define the misfit function, it is possible to consider a wavefield transformation in which the experimental and the theoretical data can be compared accounting also for higher modes of propagation in active-source data (Forbriger, 2003; Ryden and Park, 2006). If proper Fourier-Bessel expansion coefficients are used (Forbriger, 2003) they represent the complete wavefield. The inversion can then account for different signal amplitudes produced by different sources and can account for near-field signals as well as body waves.

As mentioned in Section 3.1.2 of the main text of these guidelines, inversion of effective-mode SPAC data can be achieved also via direct fitting of experimental SPAC coefficients with theoretical ones produced using effective-mode assumptions (Ikeda et al., 2012), without obtaining the experimental dispersion curve.

Full waveform inversion

In the full waveform inversion, the experimental time domain signals are compared directly to synthetic signals (e.g. Tran and Hiltunen, 2012). It allows not only for higher modes to be considered but also for a full account of the different propagation phenomena. As such, it allows near field effects to be fully captured. Although very promising, this approach is still under development and it is not yet adopted for standard applications at least in near surface characterization.

Specific References

Aki K, Richards PG (2002) Quantitative Seismology. Sausalito, CA, University Science Books

Forbriger T (2003) Inversion of shallow-seismic wavefields: II. Inferring subsurface properties from wavefield transforms. Geophysical Journal International 153: 735–752

Gabriels P, Snieder R, Nolet G (1987) In situ measurement of shear wave velocity in sediments with higher-mode Rayleigh waves. Geophysical prospecting 35: 187-196

Ganji V, Gucunski N, Nazarian S (1998) Automated inversion procedure for spectral analysis of surface waves. Journal of Geotechnical and Geoenvironmental Engineering 124: 757–770.

Herrmann RB (2007) Computer Programs in Seismology, Version 3.30. St. Louis, MO, Saint Louis University.

Ikeda T, Matsuoka T, Tsuji T, Hayashi K (2012) Multimode inversion with amplitude response of surface waves in the spatial autocorrelation method. Geophys. J. Int. 190: 541–552

Lai CG, Mangriotis M-D, Rix GJ (2014) An explicit relation for the apparent phase velocity of Rayleigh waves in a vertically heterogeneous elastic half-space. Geophys. J. Int. 199: 673–687

Lu L, Zhang B, (2006) Inversion of Rayleigh waves using a genetic algorithm in the presence of a low-velocity layer. Acoustical Physics 52: 701–712.

Lunedei E, Albarello D (2009) On the seismic noise wavefield in a weakly dissipative layered Earth. *Geophys. J. Int.* 177: 1001–1014, doi:10.1111/j.1365-246X.2008.04062.x (with the relative "Erratum", *Geophys. J. Int.* 179: 670, doi:10.1111/j.1365-246X.2009.04344.x).

Maraschini M, Ernst F, Foti S, Socco V (2010) A new misfit function for multimodal inversion of surface waves. Geophysics 75 (4): 31-43

Maraschini M, Foti S (2010) A Monte Carlo multimodal inversion of surface waves. Geophys. J. Int. 182(3): 1557-1566.

O'Neill A, Matsuoka T (2005) Dominant higher surface-wave modes and possible inversion pitfalls. Journal of Environmental and Engineering Geophysics 10: 185–201.

Ryden N, Park CB (2006) Fast simulated annealing inversion of surface waves on pavement using phase-velocity spectra. Geophysics 71(4): R49–R58.

Stokoe KH, Wright SG, Bay J, Roesset JM (1994) Characterization of geotechnical sites by SASW method, in Geophysical characterization of sites, (ISSMFE TC#10) by R.D. Woods (ed), Oxford & IBH Publ., pp. 15-25

Tokimatsu K (1997) Geotechnical site characterization using surface waves. Proc. 1st Intl. Conf. Earthquake Geotechnical Engineering, Vol. 3, 1333–1368.

Tran K, Hiltunen D (2012) Two-Dimensional Inversion of Full Waveforms Using Simulated Annealing. J. Geotech. Geoenviron. Eng. 138(9) : 1075–1090

APPENDIX 6.   – JOINT INVERSION OF SURFACE WAVE DATA AND OTHER GEOPHYSICAL DATA

As for any inverse problem, the inversion of surface wave data can benefit from the inclusion in the target function of additional available experimental data. This is often implemented with a-priori information (e.g. stratigraphic logs). An appealing possibility to improve the reliability of the final model is given by joint inversion with data given by other geophysical tests. As geophysical models sharing common parameters can be defined, the joint inversion can provide more reliable shear wave velocity profiles. A crucial prerequisite is that different material properties share the same stratigraphy. Several examples from the literature are cited in the following:

- Surface wave analysis and P-wave refraction (Piatti et al., 2013): the joint inversion, in this case, benefits from the possibilities of using a common data acquisition equipment and setup with active-source surface wave tests (Foti et al., 2003; Forbriger, 2003);

- Surface wave analysis and Vertical Electric Soundings (Hering et al., 1995; Misiek et al., 1997; Comina et al., 2001; Wisén and Christiansen, 2005): the layer thickness can be shared as coupling model parameter under the assumption that seismic interfaces are also electric interfaces;

- Surface wave analysis and Micro-gravimetric Surveys (Hayashi et al. (2005): microgravimetric data can indeed help in defining major stratigraphic features.

For example, results of a deterministic joint inversion of surface wave dispersion curve and P-wave first arrival times are reported in Figure A6-1. As P-wave refraction is highly sensitive to water table position and the latter has a strong influence on surface wave dispersion curve, the benefits of a joint inversion are mainly due to the possibility to have a reliable definition of parameters that are typically assumed a-priori (i.e. the V_P or the Poisson ratio of the layers). Comparing the profiles obtained from individual inversions of surface wave dispersion (which provides only the V_S profiles) and P- wave first arrival times (which provides only the V_P profile) with the joint inversion (which provides both profiles simultaneously), it is clear that a more reliable model is obtained with the latter, as confirmed from the comparison with local stratigraphy observed in a borehole log obtained in the vicinity of the site and reported on the velocity profiles.
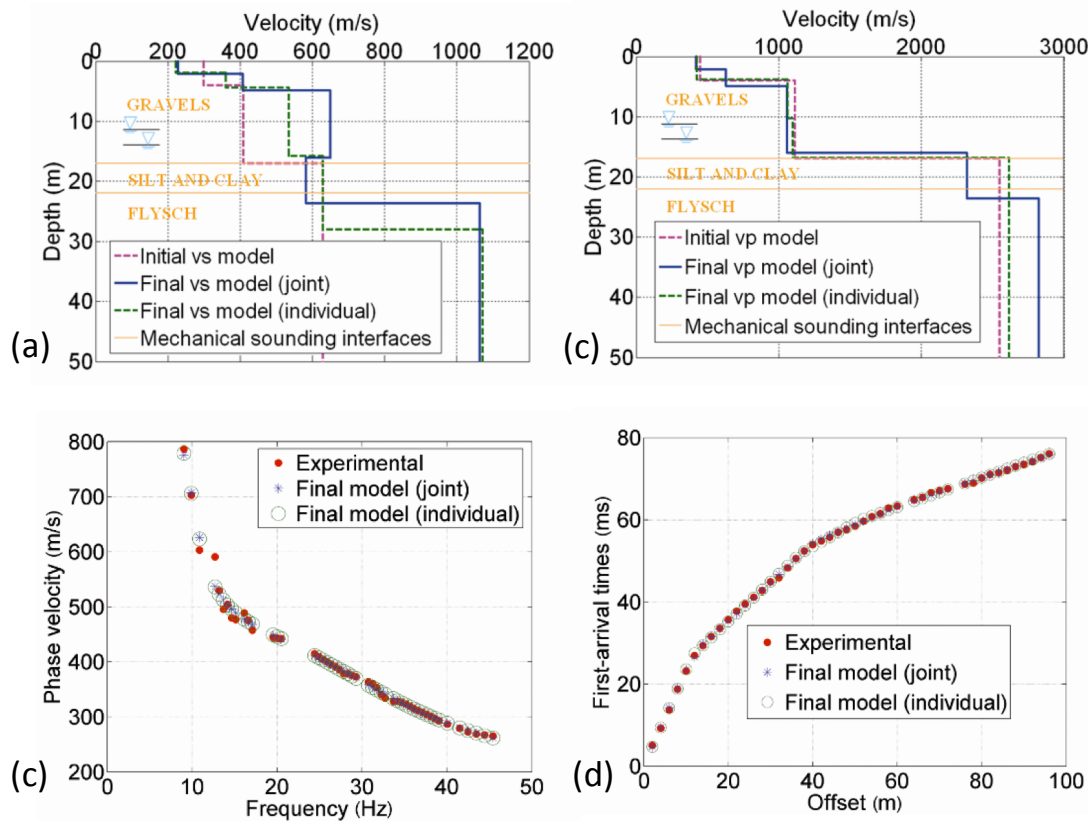
Figure A6.1 – Example of individual and joint inversions of surface wave dispersion curve and P-wave refraction first arrival times: a) V_S profile b) V_P profile c) fitting on the surface wave dispersion curve d) fitting on the P-wave first arrival times (Piatti et al., 2013)

Specific References

Comina C, Foti S, et al. (2001) Joint Inversion of VES and Surface Wave Data. Symposium on the Application of Geophysics to Engineering and Environmental Problems, SAGEEP 2001, Las Vegas , USA.

Forbriger T (2003) Inversion of shallow-seismic wavefields: II. Inferring subsurface properties from wavefield transforms. Geophysical Journal International 153: 735–752.

Foti S, Sambuelli L, Socco LV, Strobbia C (2003) Experiments of joint acquisition of seismic refraction and surface wave data. Near Surface Geophysics 1: 119-129

Hayashi K, Matsuoka T. et al. (2005) Joint Analysis of a Surface-wave Method and Micro-gravity Survey. Journal of Environmental and Engineering Geophysics 10(2): 175-184.

Hering A, Misiek R, Gyulai A, Ormos T, Dobroka M, Dresen L (1995) A joint inversion algorithm to process geoelectric and surface wave seismic data. Part I: basic ideas. Geophysical Prospecting 43: 135-156

Misiek R, Liebig A, et al. (1997) A joint inversion algorithm to process geoelectric and surface wave seismic data. Part II: applications. Geophysical Prospecting 45: 65-85.

Piatti C, Boiero D, Foti S, Socco LV (2013) Constrained 1D joint inversion of seismic surface waves and P-refraction traveltimes. Geophysical Prospecting 61 (Suppl. 1): 77–93

Wisén R, Christiansen AV (2005) Laterally and Mutually Constrained Inversion of Surface Wave Seismic Data and Resistivity Data. Journal of Envir. and Eng. Geophysics 10(3): 251–262.

APPENDIX 7.   – JOINT INVERSION OF DISPERSION CURVE AND HVSR

As stated in Section 4 of the main text of these guidelines, the inverse problem is mathematically ill-posed since it is affected by solution non-uniqueness and several different models may provide a similar fit of experimental data. To face this problem, other experimental data can be added to the dispersion curve in the inversion process (see also Appendix 6). Among these, the Horizontal-to-Vertical Spectral Ratio (HVSR or H/V) curve is of major interest. It is obtained by three-directional single-station measurements of the ambient vibration ground-motion carried out for few tens of minutes at the surface: average spectral ratios of horizontal (H) and vertical (V) ground motion components are computed to determine the curve as a function of the frequency. Detailed guidelines about H/V technique (including field procedures and processing) have been drawn in the frame of the SESAME European project (D23.12 in http://sesame.geopsy.org/SES_TechnicalDoc.htm).

In general, despite the fact that all seismic phases possibly contribute to the ambient vibrations, surface waves are reputed to play a major role in determining the shape of the H/V curve (*e.g.*, Bonnefoy-Claudet *et al.*, 2008). This implies that jointly considering H/V and dispersion curves in the inversion also allows extending the exploration depth of the survey.

The use of qualitative or semi-quantitative matching of peak frequencies or shapes of theoretical H/V curves with observed H/V curves is well established as a tool for making use of low-frequency information not available in dispersion curves. Such information improves the resolution of depth, especially for deep interfaces (e.g., Hayashi et al., 2011; Asten et al., 2014).

Formal joint inversion procedures require forward modelling of both H/V and dispersion curves. By approximating the Earth as a stack of homogeneous and isotropic layers, several numerical tools exist to model Love and Rayleigh waves dispersion curves, also accounting for higher modes (cf. Appendices 1 and 5). In the case of the H/V curve, however, several alternative models exist providing different outcomes (Herak, 2008; Lunedei & Albarello, 2009, 2015; Sánchez-Sesma *et al.*, 2011; Fäh *et al.*, 2001). In the same way, different opinions also exist in the scientific literature about the parts of the H/V curve to be included in inversion procedure: the whole curve, some parts of it or just the frequency values corresponding to H/V maxima (*e.g.*, Parolai *et al.*, 2005).
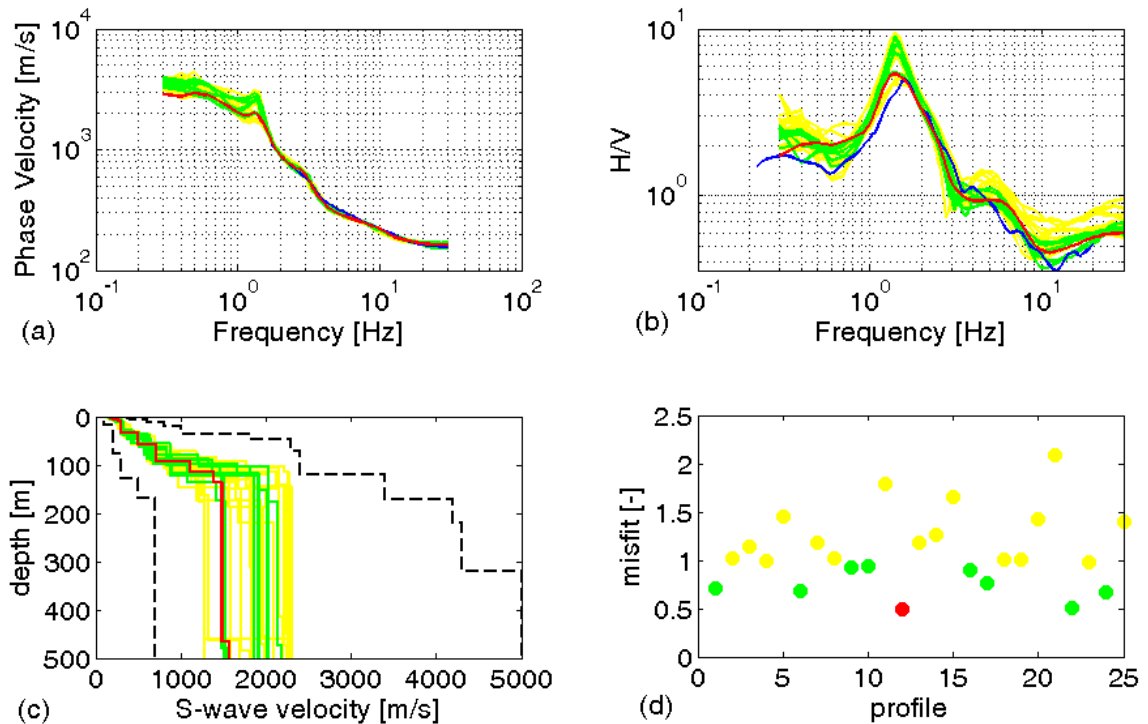
Figure A7. 1 - Example of results obtained by a joint inversion of dispersion (VR) and H/V curves. Curves are shown in top panels, while V_S depth profile and misfit values (which is the measure of the disagreement between experimental and synthetic curves) are in lower panels. Blue lines represent experimental curves. Red lines mark the quantities relative to the best profile (which has the minimum misfit value). Green lines correspond to other obtained profiles whose misfit is not higher than the double of the minimum one: these profiles are useful to estimate the variability of the result. Yellow lines are relative to the other resulting profiles. Dashed black lines in the V_S panel show the search limit adopted in this inversion procedure.

To avoid this problem, approaches have been developed in which specific phases are selected in the experimental record to perform the spectral ratio. This is the case of the polarization analyses, aiming at isolating Rayleigh wave phases and inverting the resulting Rayleigh waves ellipticity (*e.g.*, www.geopsy.org; Hobiger et al., 2013).

A joint inversion procedure also requires the definition of a single misfit function for both dispersion and H/V curve. This implies that the operator must provide suitable weights for the misfits provided by the two curves. The lack of a general agreement about the best forward model to reproduce the H/V curve and of its role in the inversion procedure has so far hampered the application of joint inversion procedures. Several academic examples exist in the scientific literature (*e.g.*, Parolai *et al.*, 2005, 2006; Picozzi, 2006; Picozzi &

Albarello, 2007; Albarello *et al.*, 2011; Pileggi *et al.*, 2011; Ikeda et al., 2013), but no commercial software is

presently available for this purpose. An example of results of a joint inversion is shown in Figure A7. 1.

<u>Specific References</u>

Albarello D, Cesi C, Eulilli V, Guerrini F, Lunedei E, Paolucci E, Pileggi D, Puzzilli LM (2011) The contribution of the ambient vibration prospecting in seismic microzoning: an example from the area damaged by the April 6, 2009 L'Aquila (Italy) earthquake. *Bollettino di Geofisica Teorica ed Applicata* 52(3): 513-538, doi:10.4430/bgta0013

Asten M, Askan A, Ekincioglu EE, Sisman FN, Ugurhan B (2014) Site Characterization in Northwestern Turkey Based on SPAC and HVSR analysis of microtremor noise.   Exploration Geophysics 45: 74-85, doi.org/10.1071/EG12026

Bonnefoy-Claudet S, Köhler A, Cornou C, Wathelet M, Bard PY (2008) Effects of Love waves on microtremor H/V ratio. *Bull. Seismol. Soc. Am.* 98(1): 288–300 doi:10.1785/0120070063

Fäh D, Kind F, Giardini D (2001) A theoretical investigation of average H/V ratios. *Geophys. J. Int.* 145:535–549

Hayashi K, Nozu A, Tanaka, M (2011) Joint inversion of three-component microtremor measurements and microtremor array measurements at Mexico City. SEG Technical Program Expanded Abstracts 2011, 917–921. doi:10.1190/1.3628222

Herak M (2008) ModelHVSR – A Matlab tool to model horizontal-to-vertical spectral ratio of ambient noise. Computers & Geosciences 34(11): 1514–1526

Hobiger M, Cornou C, Wathelet M, Di Giulio G, Knapmeyer-Endrun B, Renalier F, Bard P-Y, Savvaidis A, Hailemikael S; Bihan NL et al. (2013) Ground structure imaging by inversions of Rayleigh wave ellipticity: sensitivity analysis and application to European strong-motion sites. Geophysical Journal International 192(1): 207–229.

Ikeda T, Asten MW, Matsuoka T (2013) Joint inversion of spatial autocorrelation curves with HVSR for site characterization in Newcastle, Australia. Extended Abstracts of the 23rd ASEG Conference and Exhibition, http://www.publish.csiro.au/nid/267.htm

Lunedei E, Albarello D (2009) On the seismic noise wave field in a weakly dissipative layered Earth. *Geophys. J. Int.* 177(3): 1001–1014, doi:10.1111/j.1365 246X.2008.04062.x (Erratum doi:10.1111/j.1365-246X.2009.04344.x)

Lunedei E, Albarello D (2015) Horizontal-to-vertical spectral ratios from a full-wavefield model of ambient vibrations generated by a distribution of spatially correlated surface sources. *Geophys. J. Int.* 201: 1140–1153, doi:10.1093/gji/ggv046

Parolai S, Picozzi M, Richwalski SM, Milkereit C (2005) Joint inversion of phase velocity dispersion and H/V ratio curves from seismic noise recordings using a genetic algorithm, considering higher modes. *Geophys. Res. Lett.*, 32: L01303, doi:10.1029/2004GL021115

Parolai S, Richwalski SM, Milkereit C, Fäh D (2006) S-wave velocity profile for earthquake engineering purposes for the Cologne Area (Germany). *Bull. Earthquake Eng.*, 4:65–94, doi:10.1007/s10518-005-5758-2

Picozzi M (2005) Joint inversion of phase velocity dispersion and H/V ratio curves from seismic noise recordings, PhD Thesis, Università di Siena

Picozzi M, Albarello D (2007) Combining genetic and linearized algorithms for a two-step joint inversion of Rayleigh wave dispersion and H/V spectral ratio curves. *Geophys J. Int.* 169: 189–200, doi:10.1111/j.1365-246X.2006.03282.x

Pileggi D, Rossi D, Lunedei E, Albarello D (2011) Seismic characterization of rigid sites in the ITACA database by ambient vibration monitoring and geological surveys. *Bull. Earthquake Eng.* 9: 1839–1854, doi:10.1007/s10518-011-9292-0

Sánchez-Sesma FJ, Rodríguez M, Iturrarán-Viveros U, Luzón F, Campillo M, Margerin L, García-Jerez A, Suarez M, Santoyo MA, Rodríguez-Castellanos A (2011) A theory for microtremor H/V spectral ratio: application for a layered medium. *Geophys. J. Int.* 186: 221–225

APPENDIX 8.   – LOVE WAVE ANALYSIS

Love waves are a type of surface waves whose motion is polarized perpendicularly to the direction of propagation and lays on a plane parallel to ground surface. To be recorded, therefore, sensors with horizontal components are needed. Differently to Rayleigh wave velocity, which depends on both P and S-wave velocities, Love wave velocity only depend on the V_S profile. Love waves are always dispersive: they require the presence of at least one softer layer over the half-space (e.g. the geophysical bedrock) to be developed.

In spite of being of trivial theoretical computation, Love wave dispersion analysis is a less common practice if compared to the analysis of the vertical component of Rayleigh waves. This is historically due to two main reasons: the difficulties in implementing an artificial source capable of generating enough shear motion and the relative scarce availability of horizontal receivers in standard seismic experiments (in travel-time analysis vertical geophones are usually employed to capture the first compressional motion of the signal). As well, these limitations apply to the analysis of the radial component of Rayleigh waves.

Active Love Wave Techniques

Although Love waves have been considered in seismological studies for many years, the application of Love wave techniques to geotechnical and near-surface investigations is only recently gaining attention. Consequently, relative to Rayleigh wave techniques the literature is sparse on topics such as two-station spectral analysis (SASLW) and multi-channel analysis (MASLW) of Love waves.

To our knowledge, one of the earliest applications of Love waves for characterizing near surface V_S structure is by Mari (1984) where the goal was to estimate static corrections for SH seismic reflection data. Later, a computational basis for the spectral analysis of Love waves was presented in Guzina and Madyarov (2003). More recent publications describing the application of MASLW include Strobbia (2005), Safani et al. (2005 and 2006), Eslick et al. (2007), Hamimu et al. (2011), Dal Moro and Ferigo (2011), Xia et al. (2012) and Martin et al. (2014).

In many geologic environments, the Love wavefield is less prone to higher mode generation than the Rayleigh wavefield (Safani, et al., 2005) and modal superposition is less of an issue with Love waves (Strobbia,

2005 and Xia et al., 2012). The inversion of Love wave dispersion data is often easier and more stable than for Rayleigh wave data (Safani et al., 2005; Xia et al., 2012). In saturated sediments, it may be necessary to account for the effects of viscoelasticity on Love wave propagation (Michaels and Gottumukkula, 2010). Eslick et al. (2007) investigate the limiting thickness of the low-velocity surface layer required to record useable Love wave data. Long receiver spreads can yield high-quality Love wave dispersion data, assuming there is not significant lateral velocity variation (Xia et al., 2012). Therefore, it is often feasible to concurrently acquire both SH-wave seismic refraction data and Love wave data to image V_S structure to 30 m depth by using a longer array (e.g. 48 channels at 3 m spacing for 141 m array). Joint inversion or modeling of Rayleigh and Love wave dispersion data (fundamental mode and/or multimode) may increase the reliability of the resulting V_S model and also be used to identify anisotropy (Strobbia, 2005; Safani et al., 2005 and 2006; Hamimu et al., 2011; Dal Moro and Ferigo, 2011). Although it may be cost prohibitive to routinely acquire both Rayleigh and Love wave data for the purpose of joint inversion, there are certain types of velocity structure that are more easily characterized using Love waves (Martin et al., 2014) and, therefore, Love wave acquisition equipment should be available on field investigations and used if necessary.

As previously mentioned, applications of Love-wave methods at the geotechnical scale have a much shorter history than Rayleigh-wave based methods. For this reason, much of the basic applied research (e.g., near-field effects; optimal survey design; source-frequency limitations, such as the low-frequency limits of a hammer and plank source; strengths and limitations) have yet to be discussed in the published literature.

With the exception of the energy source and horizontal geophones (4.5 Hz recommended), the equipment and procedures for acquiring Love wave data are similar to those for Rayleigh wave data acquisition (see Section **Errore. L'origine riferimento non è stata trovata.**). A common field layout for a Love wave investigation to 30 m depth would be 24 or 48 4.5-Hz horizontal geophones spaced 3 m apart for array lengths of 69 and 141 m, respectively, or 48 geophones spaced 1.5 or 2 m apart for an array lengths of 70.5 and 96 m, respectively. The 141 m and possibly the 69 m long arrays may also be adequate to image velocity structure to 30 m depth using the S-wave seismic refraction technique. Both forward and reverse offset source locations are recommended with source offset in the 1.5 to 30 m range. Multiple source offsets may be beneficial in some cases. The addition of interior shot locations allows for seismic refraction tomography analysis and seismic records from these shot locations can also be used for surface wave analysis.

Love waves can be artificially generated by using sources (impulsive or harmonic) capable of producing displacement parallel to ground surface. One popular artificial source for Love wave generation in small-scale surveys is the shear-beam (Figure 8.1). Shear waves are here generated by side impact of a hammer (or any heavy load) on a horizontal beam (often made of wood, less frequently iron or steel) generally locked in place by some form of vertical loading (survey operators, a car, etc…). Horizontal weight-drop or pendulum-type sources can be deployed to generate lower frequency energy but can be very time-consuming to set up. Weight-drop sources that strike the ground at a 30 to 45º angle are more portable. Less frequent, due to higher costs, is the use of vibrating sources or shakers. Unlike impulsive sources, such devices are capable to generate a continuous harmonic signal at a single frequency or over a band-limited band (e.g. a sweep signal). The clear advantage of this kind of sources is, therefore, the duration, which can be increased to optimize the signal-to-noise ratio of the recordings. These devices, however, are conversely quite limited in the lowermost deliverable frequency due to technical limitations (mostly size and weight). Large, horizontal VibroseisTM energy sources are very well suited for Love-wave acquisition but are prohibitively expensive. Examples of SH-wave energy sources are shown in Figure A8. 2.
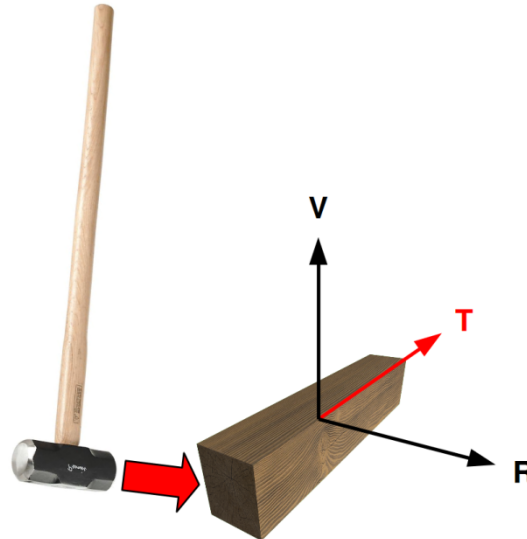
Figure A8. 1 - Schematic representation of a simple artificial source (shear beam) used to generate Love waves (transversal component T of motion).

Horizontal Traction Plank (Wood Beam)

Hammer-Impact Aluminum Shear Wave Seismic Source

United Service Alliance A100 Accelerated Impact Energy Source in S-wave Mode

Industrial Vehicles International Seismic Vibrator (courtesy of University of Texas at Austin)

Figure A8. 2 - Example of S_H wave energy sources.

Due to practical (i.e., source frequency limitations) and theoretical (i.e., lower frequency Love waves required to image to a specific depth than Rayleigh waves in many geologic conditions) considerations, active Love wave techniques are not particularly well suited to the imaging of V_S structure to 30 meter depth at soft soil sites. Fortunately, soft soil sites are generally relatively easily characterized using Rayleigh wave techniques, although there can be benefits of joint Rayleigh and Love wave inversion. Passive Love-wave techniques, however, can be useful for characterizing V_S structure of low-velocity sediment sites in urban environments. Active Love wave techniques are better suited to the imaging of 30 m deep V_S structure at stiff soil and rock sites, where a sledge hammer and horizontal-traction plank source can generate sufficient energy over the required frequency band.

Data reduction of active Love wave data is the same as that for Rayleigh wave data as summarized in Section **Errore. L'origine riferimento non è stata trovata.** of the main text of these guidelines. Inversion of

Love wave dispersion data is also similar to that of Rayleigh wave data (Section **Errore. L'origine riferimento non è stata trovata.**) but, of course, a different forward solution is required for the inversion. Martin et al. (2014) identified several types of sites that may be more easily characterized using Love wave techniques. These include sites with an abrupt increase in V_S at shallow depth (e.g. shallow rock site), sites with a steep velocity gradient and sites with a thin low velocity surface layer overlying much stiffer sediments. These types of velocity structure often excite dominant higher modes in Rayleigh wave data, but not in the Love wave data. Figure A8. 3 compares the f-v spectrum of Rayleigh and Love wave data collected at a shallow rock site. Due to the expected sharp impedance contrast at shallow depth, the first higher mode Rayleigh wave was expected to be dominant at low frequencies in which case it would have been possible to model the data using a Rayleigh wave multimode or effective mode routine. However, coherent fundamental or 1st higher mode Rayleigh wave dispersion data was not recovered at low frequencies. At this site the fundamental mode Love wave is dominant at all frequencies and, therefore, the Love wave data was used for site characterization.
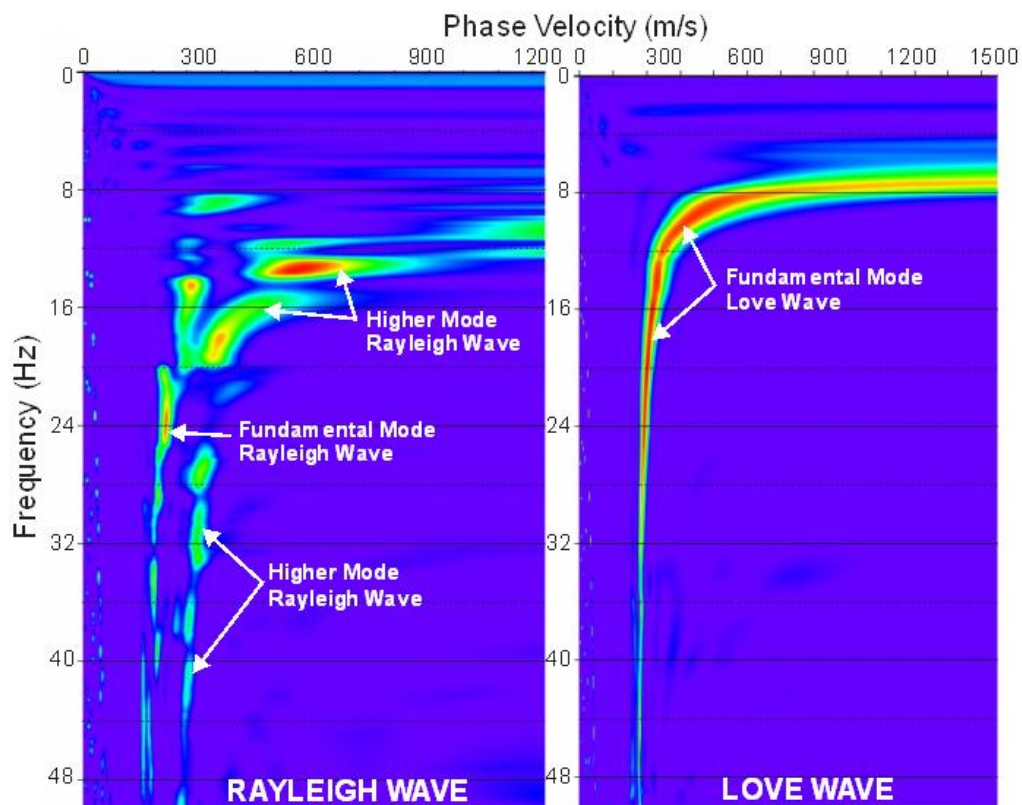

Figure A8. 3 – Rayleigh and Love wave v-f spectrums from shallow rock site
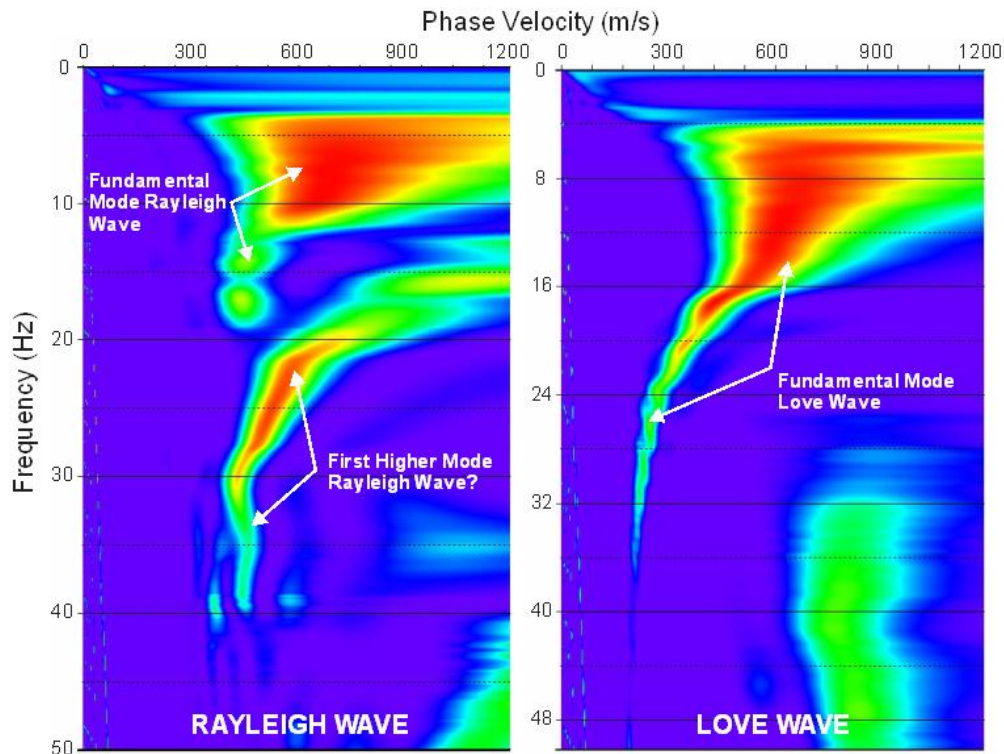
Figure A8. 4 – Rayleigh and Love wave v-f spectrums from site with low velocity surface layer overlying stiffer

sediments/soft rock

Figure A8. 4 compares the f-v spectrum of Rayleigh and Love wave data collected at a site with a thin low velocity sediment layer overlying stiffer sedimentary rock. At this site, the fundamental and 1st higher mode Rayleigh waves are dominant at low and high frequencies, respectively. Although it is plausible to conduct multimode inversion of the Rayleigh wave data at this site, inversion of the fundamental mode Love wave was less complicated. Figure A8. 5 compares the f-v spectrum of Rayleigh and Love wave data collected at a site where the velocity structure alone would predict a dominant fundamental mode Rayleigh wave yet it is not possible to recover the fundamental mode over sufficient frequency band for modeling. In fact, at a 30 m source offset, there is no evidence of the fundamental mode and the resulting dispersion curve could have easily been incorrectly modeled as fundamental mode had more data not been available. This is a good example of the benefit of multiple source offsets as the f-v spectrum from a 1.5 m source offset recovers the fundamental mode Rayleigh wave over a small frequency band. The fundamental mode Love wave was dominant at this site and, therefore, the site was characterized using the Love wave data. The expected source of the dominant higher mode Rayleigh wave at most frequencies is low velocity, high damping (low Q) sediments in the near surface.
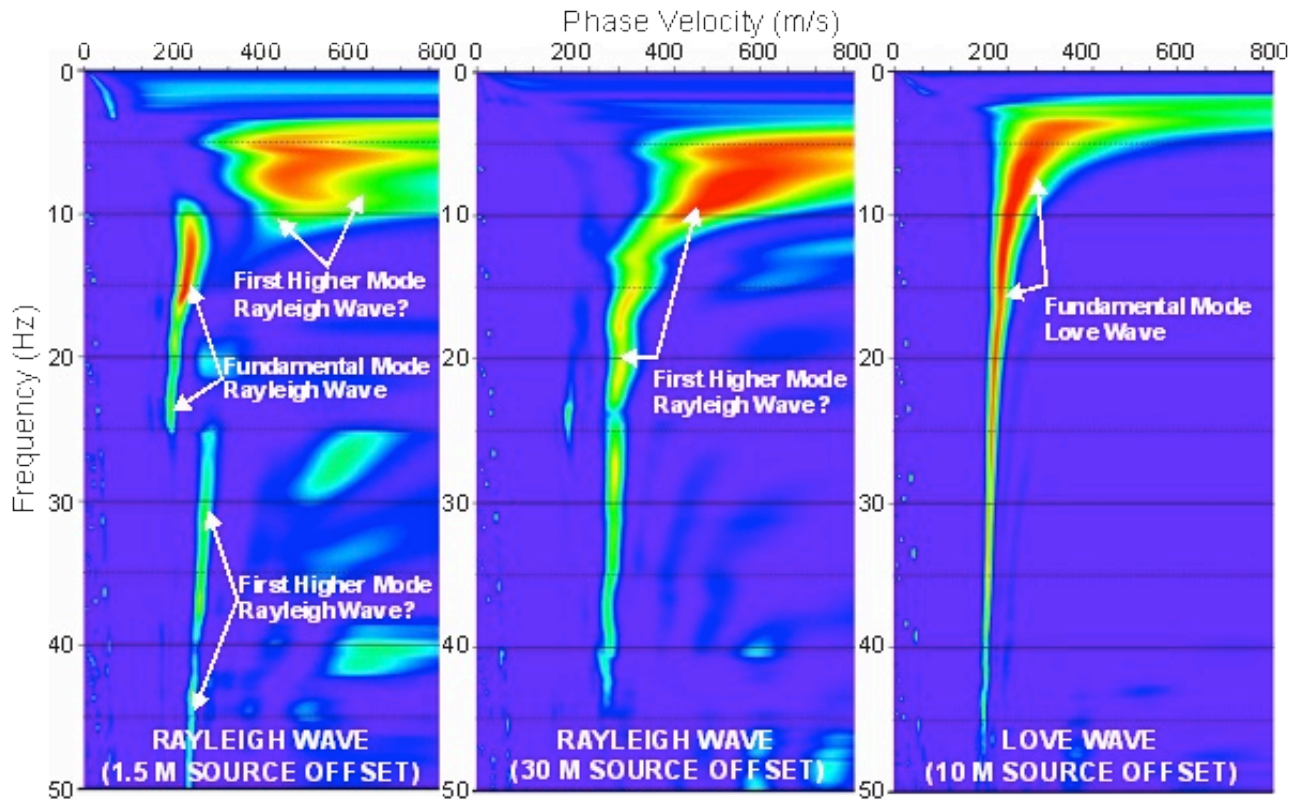
Figure A8. 5 – Rayleigh and Love wave v-f spectrums from site with low velocity, high damping (low Q) near surface sediments

Passive Love Wave Techniques

Love wave generation is clearly not an issue for passive measurements. Ambient vibration wavefield can be indeed rich of this kind of surface waves (although a unique agreement has not been reached yet by the scientific community in defining its relative proportion with respect to body and Rayleigh waves). The high-sensitivity sensors used for passive acquisition, are nowadays nearly always three-component seismometers, which give the possibility to simultaneously record and analyze the vertical and horizontal components of the ground motion. The separation of the Love and Rayleigh wave contributions in the horizontal directions is nevertheless not a trivial task in ambient vibrations, where the sources are supposedly distributed uniformly around the recording location. Fortunately, for a given direction of arrival (DOA) Love and Rayleigh waves are polarized orthogonally, that means perpendicularly and along the propagation path respectively. Therefore, if the DOA is known (or better assumed during a directional search), such ambiguity can be solved by decomposition of the wave-field into DOA-relative radial and transversal components (a process also called

directional filtering). Standard processing techniques such as f-k analysis can then be used on these components. An example of Rayleigh and Love wave dispersion curves extracted from 3-component arrays is reported in Figure A8.6.

Joint inversion of Love and Rayleigh waves dispersion curves

As mentioned, Love wave propagation is solely controlled by the S-velocity distribution of the site. Therefore, if jointly inverted with Rayleigh waves (vertical and radial component), Love wave dispersion can help reducing the non-uniqueness of the inversion problem by providing an additional constraint to the shear velocity and consequently by minimizing some of the trade-offs with the compressional velocity. An even better extension is the combined analysis of three-component surface waves, Rayleigh ellipticity and the fundamental resonance frequency of the site.

A simple inversion approach consists in performing a first inversion test using Love wave dispersion alone. The best V_S profile can subsequently be used as a priori information for the inversion of Rayleigh wave dispersion (and/or ellipticity function), allowing V_P as the only free parameter. This approach, however, is limited by the quality of the initial Love dispersion curve estimate; any uncertainty in the V_S inversion will be then propagated as an error in the V_P profile. Alternatively, Love and Rayleigh information can be inverted simultaneously, but allowing different weights to the curves depending on the sensitivity of the datasets. Unfortunately, since sensitivity can hardly be defined a priori, a number of trials is often necessary before converging to an optimal solution. As in the case of single component inversion, clearly, the presence of uncertainty in the phase dispersion, errors in mode addressing and lack of resolution in some frequency bands might limit the effectiveness of the combined approach.

Inconsistency and incompatibility between Love and Rayleigh dispersion curves are nevertheless important factors to highlight site peculiarities, such as the presence of material anisotropy (possible for example in fine-layered lacustrine sediments) or development of 2D/3D wave propagation phenomena. These cases should be handled carefully, as standard assumptions required by surface wave processing are broken, and erroneous interpretations might be produced.
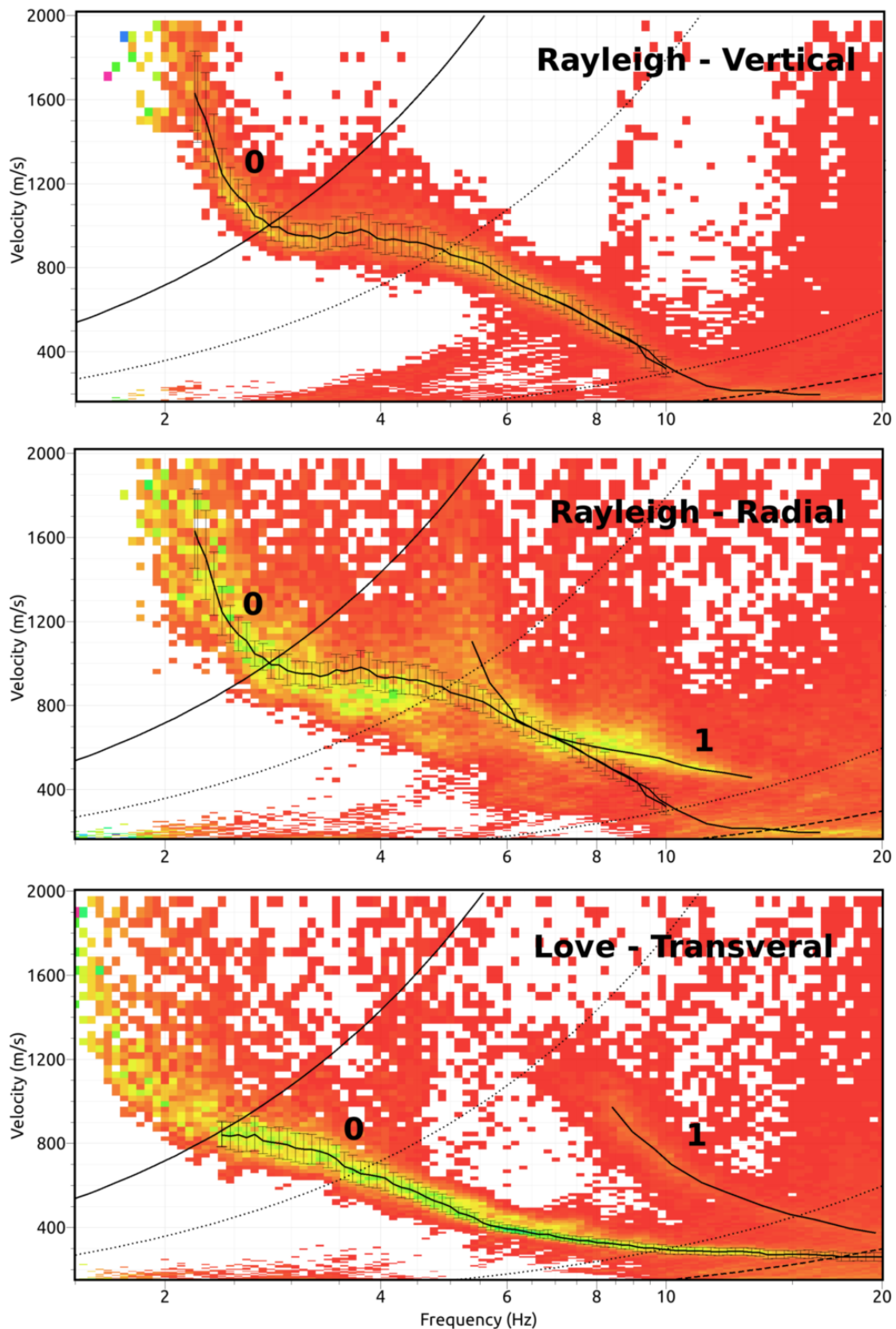
Figure A8. 6 - Example of three-component f-k array processing of ambient vibration in Brigg (Switzerland).

Love fundamental and first higher modes are better identifiable than the Rayleigh wave dispersion

on vertical component.

Specific References

Dal Moro G, Ferigo, F (2011) Joint Analysis of Rayleigh- and Love-wave dispersion curves: Issues, criteria and improvements. Journal of Applied Geophysics 75: 573-589.

Eslick R, Tsoflias G, Steeples DW (2008) Field investigation of Love waves in near-surface seismology. Geophysics 73 (3): G1–G6.

Guzina BB, Madyarov AI (2010) On the spectral analysis of Love waves. Bulletin of the Seismological Society of America 95 (3): 1150-1169.

Haines SS (2007) A Hammer-impact, aluminum shear-wave seismic source, U.S. Geological Survey Open-File Report 2007-1406, 5 p.

Hamimu L, Safani J, Nawawi M (2011) Improving the accurate assessment of a shear-wave velocity reversal profile using joint inversion of effective Rayleigh wave and multimode Love wave dispersion curves. Near Surface Geophysics 9: 1-14

Mari JL (1984) Estimation of static corrections for shear-wave profiling using the dispersion properties of Love waves. Geophysics 49: 1169–1179.

Martin AJ, Yong A, Salomone LA (2014) Advantages of active Love wave techniques in geophysical characterization of seismographic station sites – case studies in California and the Central and Eastern United States. Proceedings of the Tenth U.S. National Conference on Earthquake Engineering, Frontiers of Earthquake Engineering, July 21-25, Anchorage, Alaska.

Michaels P, Gottumukkula V (2010) Theory of viscoelastic Love waves and their potential application to near-surface sensing of permeability. Advances in Near-Surface Seismology and Ground-Penetrating Radar, Geophysical Developments Series No. 15, Society of Exploration Geophysicists, 263-280.

Safani J, O'Neill A, Matsuoka T and Sanada Y (2005) Applications of Love wave dispersion for improved shear-wave velocity imaging. J. Environ. Eng. Geophysics 10 (2): 135–150.

Safani J, O'Neill A, Matsuoka T (2006) Full SH-wavefield modelling and multiple-mode Love wave Inversion. Exploration Geophysics 37: 307-321.

Strobbia C (2005) Love wave analysis for the dynamic characterisation of sites. Bollettino di Geofisica Teorica ed Applicata 46: 135-152.

Xia J, Xu Y, Luo Y, Miller RD, Cakir R, Zeng C (2012) Advantages of using Multichannel analysis of Love waves (MALW) to estimate near-surface shear-wave velocity. Surveys in Geophysics: 841–860.

APPENDIX 9. – AMBIENT NOISE MEASUREMENTS WITH LINEAR ARRAYS

Since ambient noise sources positions are unknown the use of 2-D arrays for ambient noise measurements (e.g. circular, nested triangle, L-shaped) is preferred and will always yield more reliable results; however, there are field conditions where only linear arrays can be applied (e.g. levees, dams, roads with no intersections) and could be used for interpretation. Deep passive surface wave soundings should only be conducted using 2D arrays with linear arrays limited to a maximum depth of investigation in the 50 to 100 m range, depending on noise conditions. Linear arrays should generally only be utilized for ambient noise measurements in urban environments where the multi-directional noise criterion is likely to be satisfied. In more rural environments, a linear array oriented perpendicular to a high traffic road can often provide ambient noise data over a wide enough azimuth range to image velocity structure to 30 m depth, or more. A criterion to assess the directionality of ambient vibrations when using a linear array is proposed by Strobbia and Cassiani (2011). Ambient noise data acquired using linear arrays can be reduced using a number of techniques including the refraction microtremor (ReMi™) approach of Louie (2001); extended spatial autocorrelation (ESAC) as outlined in Chavez-Garcia, et al. (2006) and various seismic interferometry approaches (e.g. Cheng et al., 2015, Le Feuvre, et al., 2015; Mulgaria and Castellaro, 2013, Nakata, et al., 2011 and O'Connell and Turner, 2011).

In no case, noise should be generated by walking or driving along the array in a low noise environment as there is no way of estimating the reliability of the resulting dispersion curves. Instead, active source techniques, such as MASW, should be utilized if there is not enough ambient noise to successfully utilize passive surface wave techniques. It is recommended that active surface wave data (MASW or SASW) be always acquired in conjunction with passive linear array data. First, the active surface wave data will provide dispersion data at higher frequencies/small wavelengths allowing shallow velocity structure to be better characterized. Secondly, good agreement between the active and passive surface wave data in the overlapping frequency band increases confidence in the accuracy of the dispersion curve estimated using a linear passive array.

Because we expect that linear arrays will only be utilized for relatively shallow investigations, similar equipment will be utilized as for MASW investigations (i.e. engineering seismograph, seismic cables, 4.5- or 2-Hz vertical geophones). A 24 channel linear array with 6 to 10 m geophone spacing is commonly utilized with

the length of the array on the order of twice the desired depth of investigation. At least 10 to 15 minutes of ambient noise data should be recorded with a sample rate of 2 ms being more than adequate.

Analysis of ambient noise measurements using ReMi™ involves the application of a slant stack transform in both the forward and reverse directions to convert seismic data from the time-offset domain (t-x) to the frequency-slowness (f-p) domain. The f-p images from the forward and reverse direction transforms are combined and the Rayleigh wave dispersion curve picked as the lower envelope of the surface wave energy. This process is subjective and there may be differences in dispersion curves picked by different analysts, especially at lower frequencies where the error is much greater. It is important to make a realistic appraisal of data quality, especially at low frequencies, and limit the use of the data and depth of investigation accordingly. Figure A9-1 illustrates p-f images from passive surface wave data analyzed using the ReMi™ technique that yields reliable and unreliable dispersion curves, respectively. Figure A9-2 provides an example of dispersion curves interpreted by multiple analysts from a single ReMi™ data set (one linear leg of an L-shaped array used as reference) collected in an environment thought to be conducive to the application of a linear passive array. At this site the ReMi™ interpretation by multiple analysts would yield a reasonably reliable estimate of $V_{S,30}$ because there is not significant scatter in the dispersion curves at wavelengths less than 60 m; however, the velocity models below 30 m depth would be significantly different because there is significant scatter in the dispersion curves at longer wavelengths. The interpreted dispersion curve from an L-shaped, which does not suffer from the subjective nature of ReMi™ interpretation, is shown for reference.

The analysis of linear array passive data using the ESAC technique is the same as that for 2D arrays, with the dispersion curve estimated by fitting a Bessel function of the first kind, order zero to the SPAC coefficients. Estimation of the dispersion curve is not subjective; however, the dispersion curve will only be correctly estimated if the multi-directional noise criterion is satisfied.
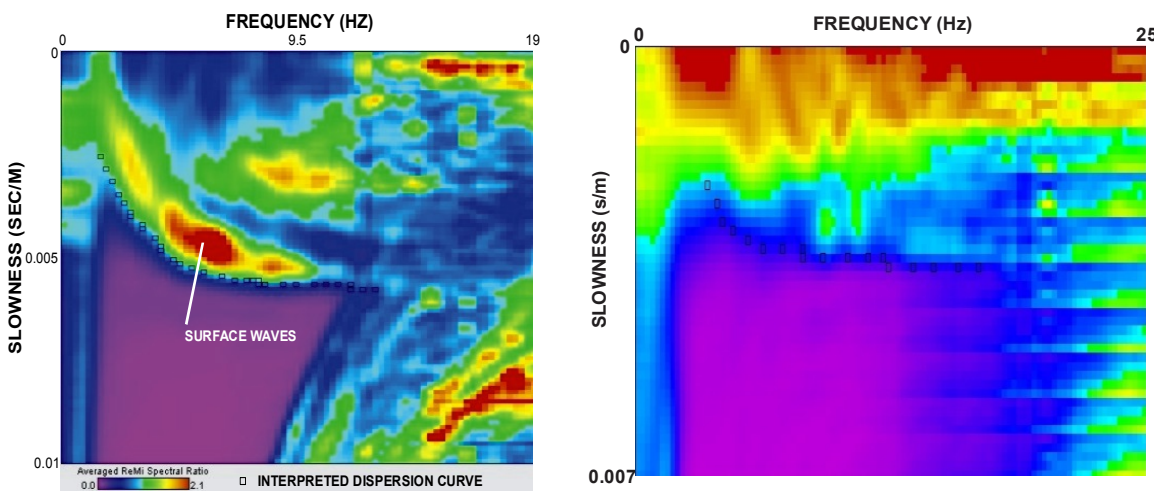
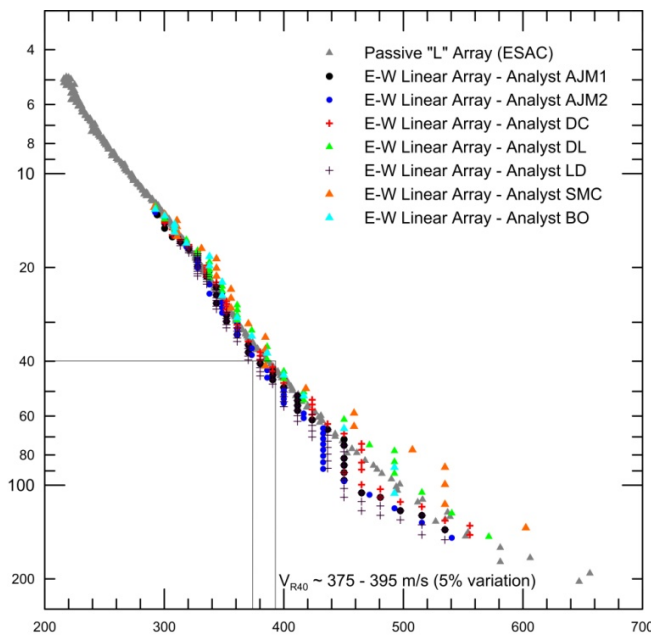*Figure A9-1. Reliable (left) and unreliable (right) dispersion curves estimated using the ReMi™ technique.*

Figure A9-2. Linear array passive surface wave data picked by multiple analysts from one linear leg of an "L" array using the ReMi™ technique

Due to the larger uncertainty estimating dispersion curves from linear array passive data relative to 2D arrays, it is recommended that dispersion curves be estimated using two techniques (e.g. ReMi™ and ESAC). If the resulting dispersion curves are in good agreement then it is likely safe to assume that the dispersion curves are reliable. Figure A9-3 shows dispersion curves from a site where active-source MASW data and passive surface wave data using both a nested triangle array and linear array were acquired with the passive linear array data analyzed using both the ReMi™ and ESAC techniques. At this specific site there is good

agreement between dispersion curves from 1) the passive and active surface wave data in the overlapping frequency band, 2) both ReMi™ and ESAC analysis of the passive linear array data and 3) passive linear and nested triangle arrays. At this site, it was concluded that all dispersion curves were accurately recovered and, therefore, all were combined at utilized for site characterization.
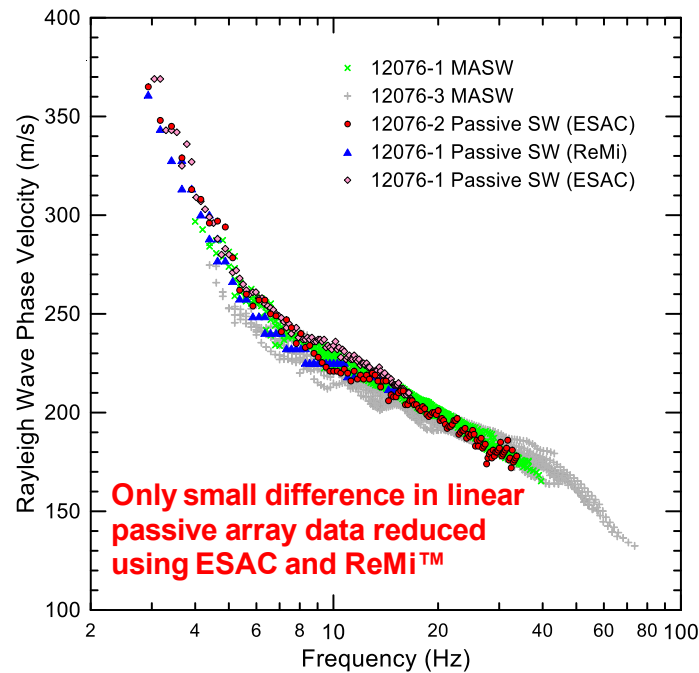

Figure A9-3. Comparison of dispersion curves from MASW data (arrays 12076-1 and 12076-3), passive linear array data (array 12076-1) and passive nested triangle array data (array 12076-2)..

Specific References

Chavez-Garcia FJ, Rodriguez M, Stephenson WR (2006) Subsoil structure using SPAC measurements along a line. Bulletin of the Seismological Society of America 96: 729–736.

Cheng F, Xia J, Xu Y, Xu Z, Pan Y (2015) A new passive seismic method based on seismic interferometry and multichannel analysis of surface waves. Journal of Applied Geophysics 117: 126-135.

Louie J (2001) Faster, better: Shear-wave velocity to 100 meters depth from refraction microtremor arrays. Bulletin of the Seismological Society of America 91: 347–364.

Le Feuvre M, Joubert A, Leparoux D, Côte P (2015) Passive multi-channel analysis of surface waves with cross-correlations and beamforming: Application to a sea dike. Journal of Applied Geophysics 114: 36-51.

Mulargia F, Castellaro S (2013) A seismic passive imaging step beyond SPAC and ReMi. Geophysics, 78 (5): KS63-KS72.

Nakata N, Snieder R, Tsuji T, Larner K, Matsuoka T (2011) Shear wave imaging from traffic noise using seismic interferometry by cross-coherence. Geophysics 76 (6): SA97-SA106.

O'Connell DRH, Turner JP (2011) Interferometric multichannel analysis of surface waves (IMASW). Bulletin of the Seismological Society of America 101 (5): 2122–2141.

Strobbia C, Cassiani G (2011) Refraction microtremors: Data analysis and diagnostics of key hypotheses. Geophysics 76(3): MA11-MA20

APPENDIX 10. – SURFACE WAVE ATTENUATION AND MATERIAL DAMPING

The attenuation of surface waves can be analysed to obtain information on the dissipative behavior of the subsoil. Indeed the same conceptual scheme adopted for the evaluation of the velocity model can be extended to the evaluation of the material damping (or equivalently the quality factor). Likewise, seismologists have inferred the quality factor structure of the Earth from the inversion of an attenuation curve measured from processing the earthquake seismograms (Aki and Richards, 2002; Romanowicz, 2002).

Surface wave attenuation with distance from the source is in fact associated with the combination of geometric attenuation (due to the spreading of energy in space) and material attenuation (due to the internal dissipation of energy during the propagation of the wave). The latter can be analysed to estimate the dissipative properties of the medium.

The three-step procedure of surface wave analysis is extended as follows: from the field data (either from active prospecting or passive surveys), an attenuation curve (i.e. material attenuation as a function of frequency) is obtained with specialized signal processing approaches. Then an inverse problem aimed at the construction of a representative model of the subsoil, including dissipation parameters, is solved (Figure A10-1).

The reference model is typically 1D, i.e. a stack of homogenous linear visco-elastic layers, and the forward problem solution can be obtained by extending the matrix procedures adopted for the elastic case (e.g. Lai and Rix, 2002).

The analysis of surface waves for building the velocity and damping models can be coupled or uncoupled. In the uncoupled approach (Figure A10-1), the attenuation curve is obtained and inverted separately from the dispersion curve. The advantage of such procedure is that the velocity model is available and it can be used to account for the geometric attenuation in the evaluation of the material attenuation curve (Rix et al., 2000). However, the coupling between surface wave phase velocity and attenuation is neglected.
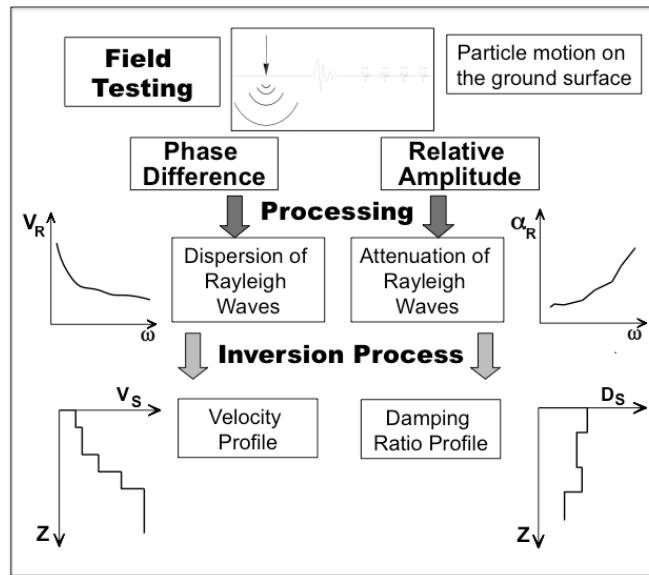
Figure A10-1. Uncoupled analysis of surface wave dispersion and attenuation.

In a fully coupled approach (Figure A10-2), the dispersion and attenuation curves are simultaneously obtained with a specific signal processing procedure. A procedure based on the transfer function approach (Oppenheim and Willsky, 1997) has been proposed by Rix et al (2001) for controlled harmonic sources and by Foti (2003) for impact sources. Then the inversion process is solved with a coupled procedure aimed simultaneously at the full set of parameters of the visco-elastic model (i.e. shear wave velocity and damping ratio of each layer) (Lai et al., 2002).
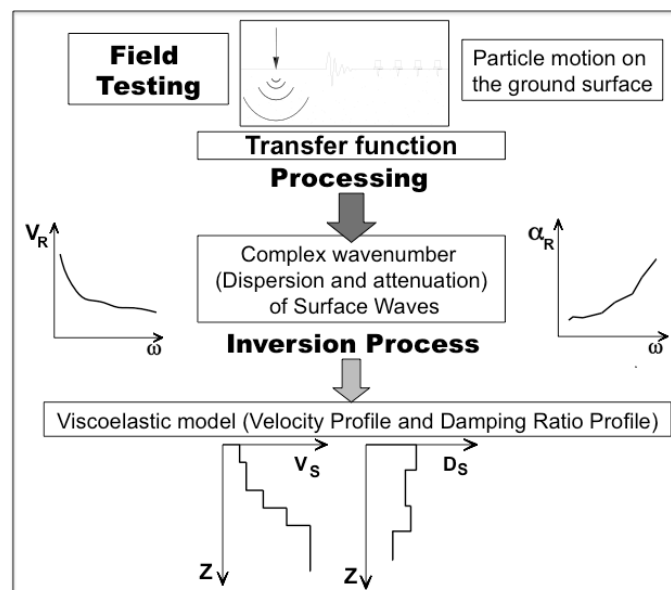

Figure A10-1. Coupled analysis of surface wave dispersion and attenuation.

Several examples of successful application are reported in the literature (Xia et al., 2002, 2012; Badsar et al., 2010, 2011). The main issues are related to the problem of a correct separation of geometrical attenuation and material attenuation, taking also into account the role of the different modes of propagation (Rix et al., 2000). Moreover, it has to be taken into account the relevance of receivers calibration as the amplitude of the particle motions is crucial for these applications.

Finally, it has to be considered that scattering of energy due to heterogeneities and lateral variation may contribute to surface wave attenuation. Since these effects are not accounted for in the forward model adopted for the inversion of the attenuation curve, an overestimation of material damping could be obtained, especially for shallow layers, as these effects are prevalent in the high-frequency range (Foti, 2004).

Specific References

Badsar SA, Schevenels M, Haegeman W, Degrande G (2010) Determination of the material damping ratio in the soil from SASW tests using the half-power bandwidth method. Geophys. J. Int. 182 (3): 1493-1508

Badsar SA, Schevenels M, Haegeman W, Degrande G (2011) Determination of the Material Damping Ratio in the Soil from SASW Test Using the Half-power Bandwidth Method and the Arias Intensity. In 8th International Conference on Structural Dynamics, Proceedings, ed. Guide De Roeck, G Degrande, G Lombaert, and G Müller. Ghent, Belgium: Ghent University, Department of Civil engineering.

Foti S (2003) Small Strain Stiffness and Damping Ratio of Pisa Clay from Surface Wave Tests. Geotechnique 53: 455-461.

Foti S (2004) Using Transfer Function for Estimating Dissipative Properties of Soils from Surface Wave Data. Near Surface Geophysics 2 (4): 231-240

Lai CG, Rix GJ, Foti S, Roma V (2002) Simultaneous measurement and inversion of surface wave dispersion and attenuation curves. Soil Dynamics and Earthquake Engineering 22(9-12): 923-930.

Lai CG, Rix GJ (2002) Solution of the Rayleigh Eigenproblem in Viscoelastic Media. Bulletin of the Seismological Society of America 92(6): 2297–2309.

Oppenheim AV, Willsky AS (1997) Signal and systems. Prentice-Hall, New Jersey

Rix GJ, Lai CG, Spang AW (2000) In situ measurements of damping ratio using surface waves. Journal of Geotechnical and Geoenvironmental Engineering 126: 472-480.

Rix GJ, Lai CG, Foti S (2001) Simultaneous Measurement of Surface wave dispersion and attenuation curves. Geotechnical Testing Journal 24: 350-358.

Xia J, Miller RD, Park CB, Tian G (2002) Determining Q of near-surface materials from Rayleigh waves. Journal of Applied Geophysics 51 (2): 121-129

Xia J, Xu Y, Miller RD, Ivanov J (2012) Estimation of near-surface quality factors by constrained inversion of Rayleigh-wave attenuation coefficients. Journal of Applied Geophysics 82: 137-144

APPENDIX 11. – EXAMPLE OF A STANDARD REPORT

This appendix provides an example of "standard" report from a rather comprehensive surface wave survey. The study is here focused on fundamental Rayleigh mode processing to be coherent with the present guidelines main text. The figures and tables are to be considered as the "minimum necessary" in order to evaluate if the survey was performed at the state of the art and to assess the quality of the recorded data as well as the robustness of study outcomes. For the sake of compactness, we do not represent all the figures or tables that may be mandatory in a "real" report (e.g. we provide power spectra of only one array whereas a complete report needs to present them for all arrays).

1. CONTEXT AND OBJECTIVE OF THE STUDY

The present work consisted in processing array passive seismic data (Ambient Vibration Array, AVA) and linear active seismic data (Multichannel Analysis of Surface Waves, MASW), in order to fill in the metadata of seismological stations from the French Accelerometric Network (RAP) with V_S vertical seismic profiles and $V_{S,30}$ values. This report shows the results at station OGBL, Le Bourget du Lac, France (73).

1.1. INVOLVED INSTITUTIONS

Client : […]

Supervision : […]

Contractor : […]

1.2. INVOLVED PEOPLE

[…]

1.3. GENERAL INFORMATION AND GEOLOGICAL SETTINGS

In this section, geographical location and geological context should be given:

The OGBL site is located in the narrow Bourget lake valley filled in with recent alluvial deposits ("Fz" geological unit in Figure A11.1) overlaying Oligocene deposits ("G3"). Some but not all geological logs of the area mentioned on the InfoTerre website indicate a peat layer in the first few meters.
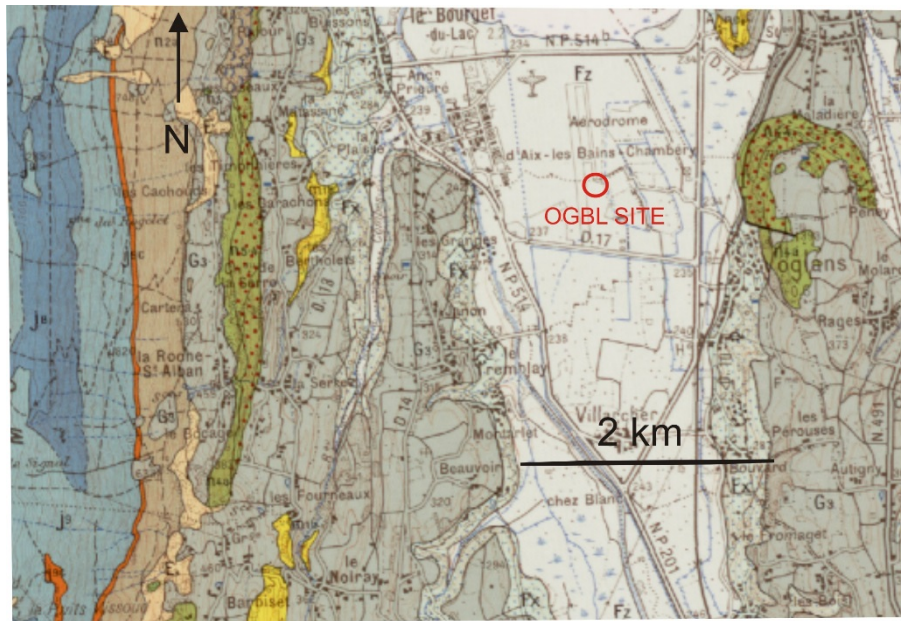
Figure A11.1: Geological Map of site measurements from InfoTerre (http://www.infoterre.brgm.fr/)

2. METHODOLOGY OF ACQUISITION AND ANALYSIS

In this section, some theoretical information about the methodology used in the study should be given in order to understand the results in the following chapters.

2.1. MULTICHANNEL ANALYSIS OF SURFACE WAVES

[…]

2.2. AMBIENT VIBRATION ARRAY

[…]

2.3. DISPERSION CURVE INVERSION

[…]

2.4. H/V SPECTRUM

[…]

3.   DATA ACQUISITION

3.1. DESCRIPTION OF EQUIPMENT

In this section, the description of the sources and receivers used in the study should be given.

3.1.1. MASW

[…]

3.1.2. Ambient vibrations

[…]

3.2. DESCRIPTION OF MEASUREMENTS

The source-receiver geometry for active (number of receivers, receiver spacing, offset of sources) and passive (shape and size of array, coordinate of each receiver) is given as well as the acquisition parameters used in the study.

Five circular seismological arrays, composed of fifteen or ten sensors each, and having different apertures were deployed for the ambient noise recordings (Figure A11.2). One linear array with 24 sensors and 46 m length was deployed for active surface wave measurements (MASW). Sensors coordinates for circular arrays are given in Table A11.1; acquisition parameters are detailed in Table A11.2.

Figure A11.2: Location map of seismic data measurements (GOOGLE EARTH). Circles indicate location of seismic stations and triangles indicate MASW profile ends

Table A11.1: Geographical coordinates of seismological stations for all arrays. (N.B. only one array is illustrated as example).

ARRAY	SENSOR	X_L93 (m)	Y_L93 (m)
R1R2	CN02	924673.36	6507969.72
	CN03	924663.11	6507957.85
	CN04	924660.18	6507961.64
	CN06	924664.69	6507962.68
	CN07	924650.68	6507964.25
	CN08	924678.22	6507956.25
	CN09	924659.81	6507972.38
	CN10	924670.21	6507945.1
	CN12	924667.86	6507955.49
	CN13	924660.42	6507953.95
	CN14	924650.05	6507952.43
	CN15	924667.91	6507960.16
	CN16	924658.24	6507958.5
	CN17	924658.69	6507943.83
	IR03	924664.3	6507953.07
….	……	……	……

Table A11.2: Acquisition parameters.

	Number of Sensors	Aperture (m)	Cut-off frequency	Sensor and digitizer types	Begin time (UTC)	End time (UTC)	Environment	Topography	Weather conditions
Array R1R2	15	10 m & 30 m	0.033 Hz	CMG6TD	18/07/2014 8h00	18/07/2014 10h00	Industrial	-	-
Array R2R3	15	30 m & 68 m	0.033 Hz	CMG6TD	18/07/2014 9h00	18/07/2014 11h00	Industrial	-	-
Array R4	10	150 m	0.033 Hz	CMG6TD	25/11/2014 9h00	25/11/2014 10h	Industrial	-	-
Array R5	10	270 m	0.033 Hz	CMG6TD	25/11/2014 10h	25/11/2014 13h00	Industrial	-	-
Array R6	10	1100 m	0.033 Hz	CMG6TD	25/11/2014 13h00	25/11/2014 16h00	Industrial	-	-
MASW	24	46 m	4.5 Hz	MarkProducts & Geode Geometrics	18/07/2014	18/07/2014	Industrial	-	-

4. PROCESSING RESULTS

4.1. POWER SPECTRA AND H/V

In order to compute power spectral densities and H/V curves, signals were cut in time windows of 50s duration. Computed Fourier amplitude spectra were smoothed using the Konno and Ohmachi (1998) procedure with a b-value of 40. The two horizontal components were then combined by computing their quadratic mean and average H/V ratios were computed by averaging the H/V ratios obtained on individual windows.

Figure A11.3 shows the power spectral density for each component at all sensors for each array. *(N.B. only the first array is illustrated as example)*
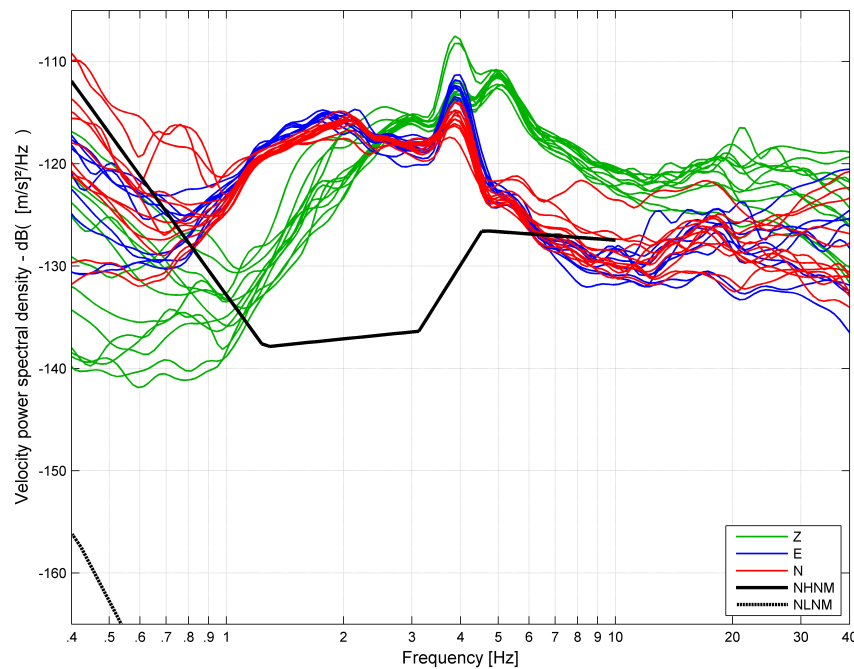

Figure A11.3: Power spectral density recorded at all sensors on the vertical (Z, green curves), North (N, red curves) and East (E, blue curves) compared to "new high noise model" (NHNM) and "new low noise model" (NLNM). The overall level of ambient vibration on the current site is very high, higher than NHNM on almost the whole frequency band of interest. (N.B. only the first array is illustrated as example).

All arrays exhibit lower spectral density on the vertical component compared to the horizontal ones between 0.3 and 1.5 Hz.
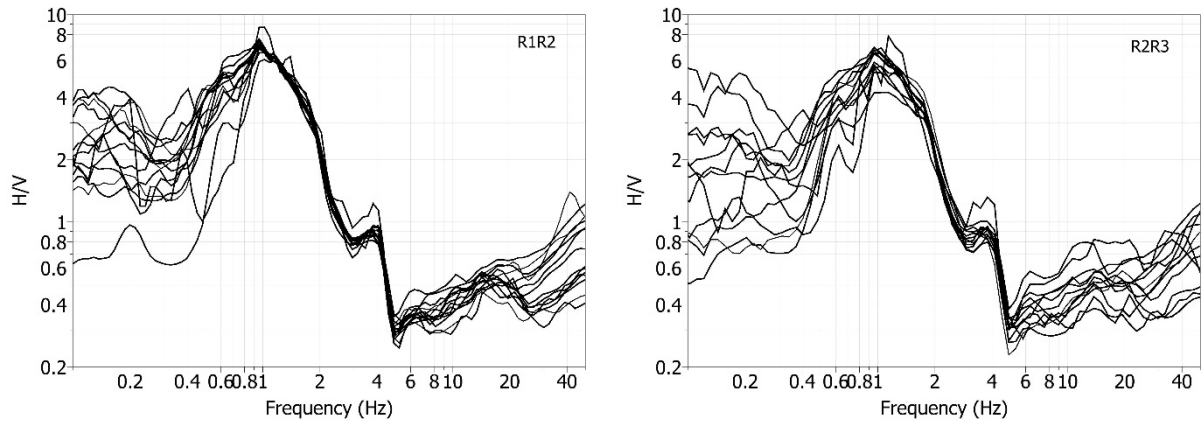
Figure A11.4: Average H/V curves observed at the different arrays. (N.B. only two arrays are illustrated as example).

Figure A11.4 reports average H/V curves obtained at all the sensors for each array. *(N.B. only two arrays are illustrated as examples).* H/V curves are very similar from one station to the other, and from array R1 R2 to the array R6, indicating a 1D velocity structure below these arrays. For these five arrays, H/V peak frequency is about 1Hz.

4.2. AMBIENT VIBRATION ARRAY MEASUREMENTS

- **FK and HRFK techniques:**

Processing parameters used for the FK and HRFK techniques applied on vertical components are indicated in Table A11.3 and Table A11.4, respectively. Phase velocity histograms (probability density functions) derived at each array are displayed in Figure A11.5, together with the extracted dispersion curve.

Table A11.3: FK processing parameters

Array	Array aperture	Window length (number of times the center period T)	Minimum frequency (Hz)	Maximum frequency (Hz)	Number of frequency bands	Minimum velocity (m/s)	Band witdh
R1R2	10 m & 30 m	100 T	0.1	20	200	50	0.1
R2R3	30 m & 68 m	50 T	0.1	15	150	50	0.1
R4	150 m	50 T	0.1	20	100	50	0.1
R5	270 m	50 T	1	20	100	50	0.1
R6	1100 m	50 T	0.1	20	100	50	0.1

Table A11.4: HRFK processing paramters

Array	Array aperture	Window length (number of times the center period T)	Minimum frequency (Hz)	Maximum frequency (Hz)	Number of frequency bands	Minimum velocity (m/s)	Band witdh
R1R2	10 m & 30 m	50 T	2	15	100	70	0.1
R2R3	30 m & 68 m	50 T	2	15	50	70	0.1
R4	150 m	100 T	0.1	20	100	50	0.05
R5	270 m	100 T	0.1	20	100	50	0.05
R6	1100 m	100 T	0.1	20	100	50	0.05

The Figure A11.5 shows the FK and HRFK maps with the picked phase velocity for each array. *(N.B. only the first and the last arrays are illustrated as examples).*
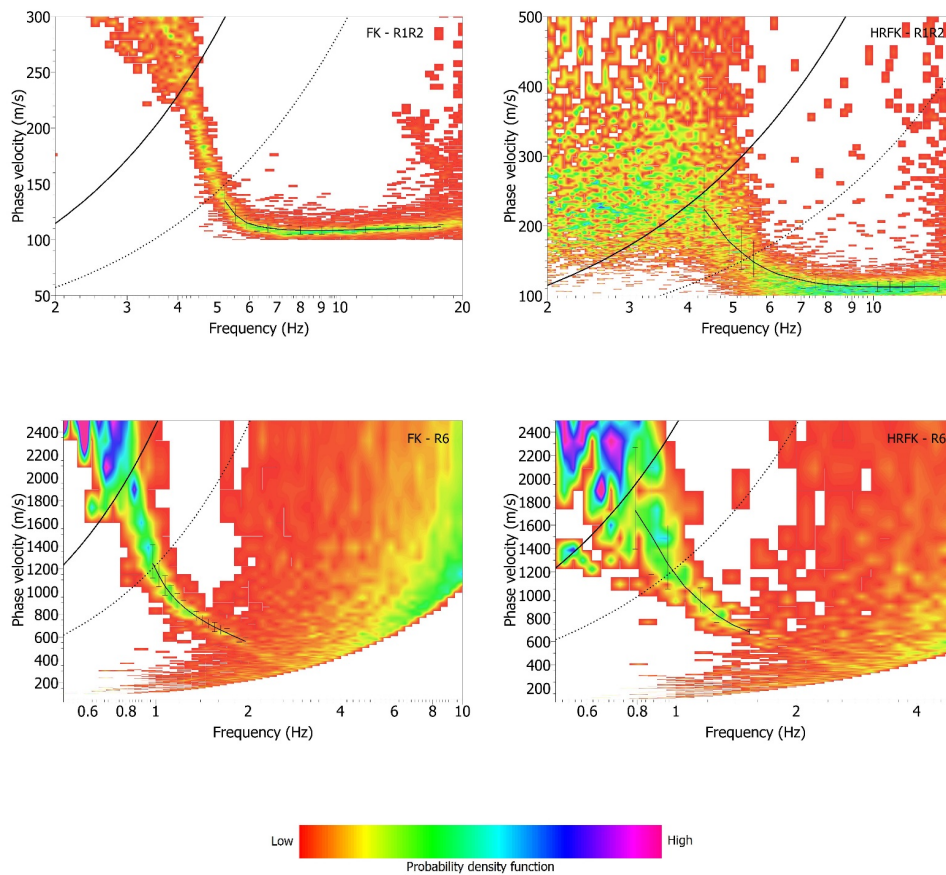

Figure A11.5: Histogram of Rayleigh wave phase velocities obtained by using FK (left panel) and HRFK (right panel) techniques for each ARRAY. The magenta and red colors indicate the highest and the lowest values of probability density function, respectively. Black dots indicate average Rayleigh wave dispersion curve +/- standard deviation. The dashed and continuous black lines indicate he theoretical array resolution limits, namely k_{min} and $k_{min}/2$. (N.B. only 2 arrays are illustrated as example)

- **MSPAC technique**

Processing parameters used for the MSPAC technique are indicated in **Errore. L'origine riferimento non è stata trovata.**. MSPAC curves obtained at the different rings for all the arrays (vertical component) are displayed in Figure A11.6. The corresponding dispersion images and picked dispersion curves are shown in Figure A11.7.
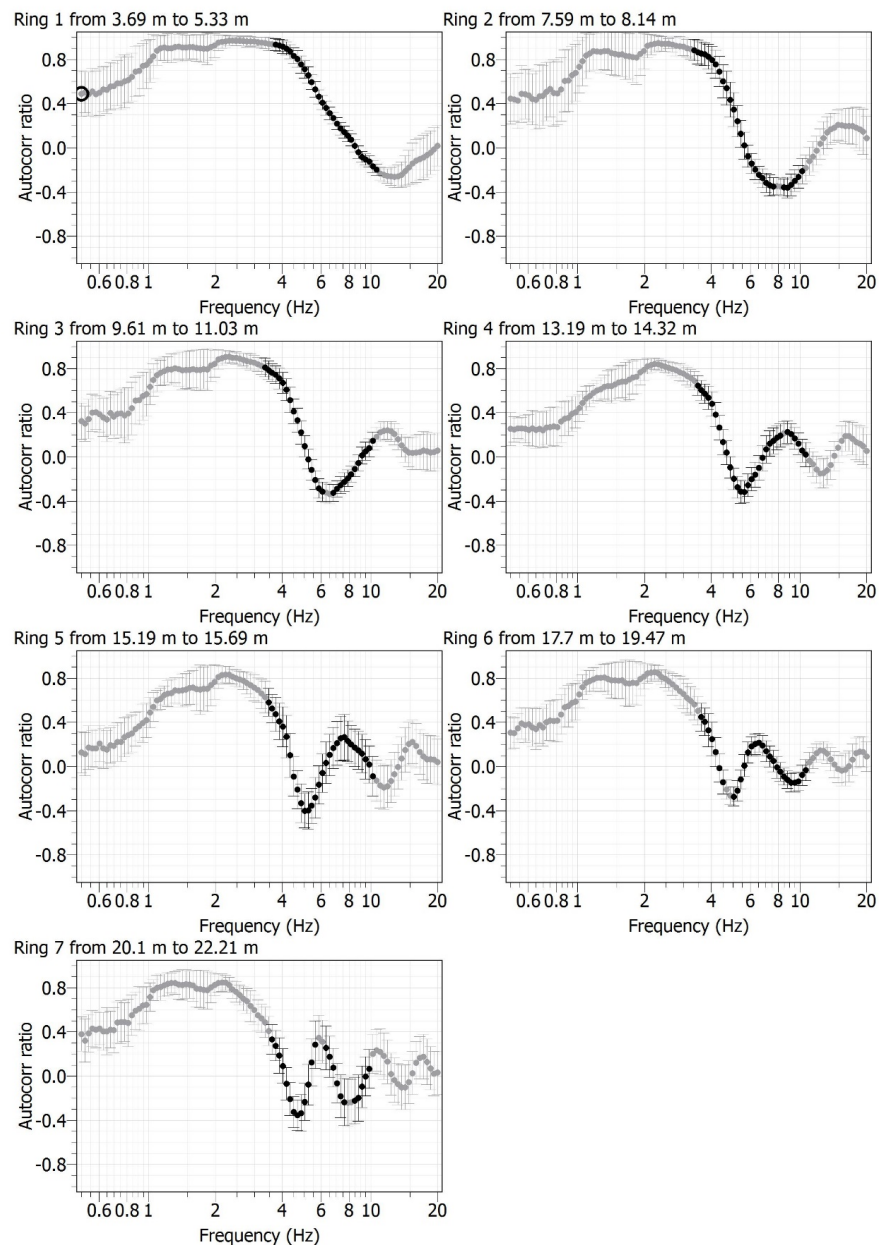

Figure A11.6:   MSPAC curves for ARRAY R1R2 (N.B. only one array is illustrated as example).
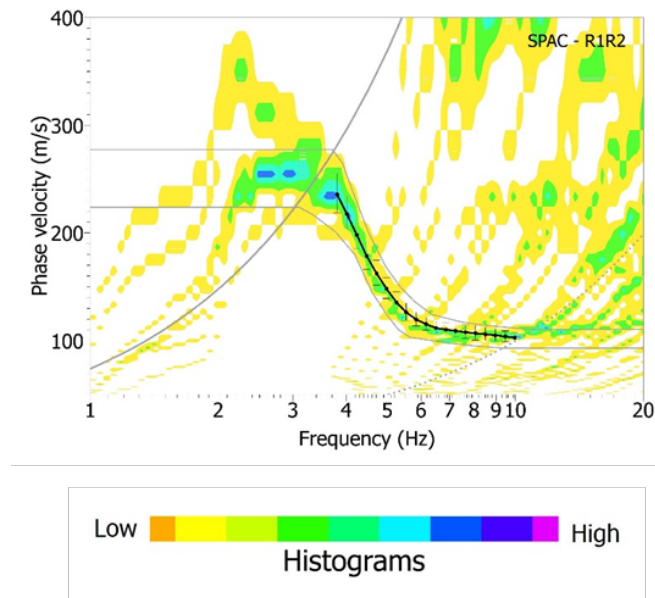
Figure A11.7: Rayleigh wave phase velocity histograms derived from MSPAC auto-correlation ratios for each

array and average dispersion curve +/- standard deviation (black dots). (N.B. only the first array is

illustrated as example).

Table A11.5:　　　MSPAC processing parameters. (N.B. only two arrays are illustrated as example).

Array	Array aperture	Window length (number of times the center period T)	Minimum frequency (Hz)	Maximum frequency (Hz)	Number of frequency bands	Nimber of rings	Minimum ring thickness (m)	Maximum ring thickness (m)	Number of pairs
R1R2	10 m & 30 m	50 T	0.5	40	50	7	3.69 7.59 9.61 13.19 15.19 17.7 20.1	5.33 8.14 11.03 14.32 15.69 19.47 22.21	14 7 18 12 5 16 5
….	….	….	….	….	….	….	….	….	….
R6	1100 m	50 T	0.1	20	100	6	220.91 390.46 503.45 606.12 750.53 894.38	319.03 445.1 559.07 707.68 850.51 1114.87	5 10 5 7 9 9

4.3. ACTIVE SURFACE WAVES TECHNIQUE (MASW)

Acquisition parameters of the MASW survey are indicated in Table A11.6. Source offset was 4 and 16 m

at each side of the profile (hereafter "forward direction" and "reverse direction" shooting). Each source offset

location involved 10 shots repetitions. Phase velocities for active surface wave data were estimated using the f-

k technique. Time series corresponding to source-to-receiver distances larger than 10 meters were used in order to reduce near-field effects (Socco and Strobbia, 2004). For each source offset distance, beampowers obtained from different shots were stacked and phase velocities corresponding to the maximum beampower were manually picked (Figure A11.8). Only phase velocities above 5 Hz were picked due to low signal-to-noise ratio at lower frequencies. Phase velocities obtained at each source location were then averaged in order to get a mean dispersion curve and its related uncertainty.

Table A11.6: MASW acquisition parameters

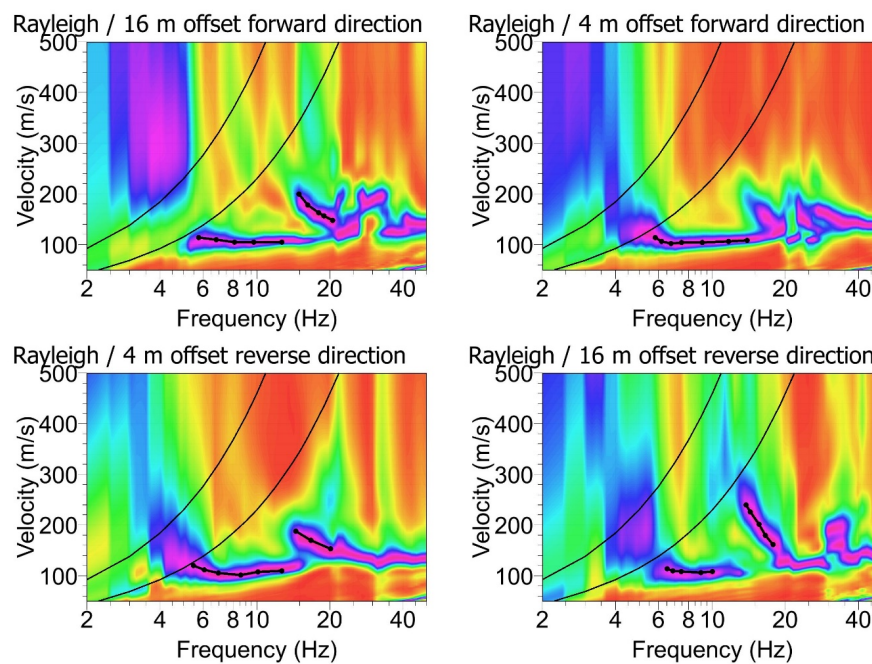| Source Offset	Geophone spacing	Hammer Weight	Source type
4 m & 16 m at each side of the profile (labelled "forward" and "reverse" shots)	2m	4,5 kg	Vertical

Figure A11.8: Beam power observed at various source offset locations for Rayleigh wave phase. The beampower was obtained by stacking beampowers obtained for individual shots. The beampower is normalized for each frequency by the maximum of the beampower. Black dots indicate the dispersion curve identified on each of the figures.

4.4. SHEAR-WAVE VELOCITY INVERSION

4.4.1. Derivation of a broad-band dispersion curve

Dispersion curves obtained from the various processing techniques are shown in Figure A11.9. They are all very consistent within their overlapping frequency band. All curves were averaged to obtain a single broad-band dispersion curve of the fundamental Rayleigh wave (Figure A11.10).
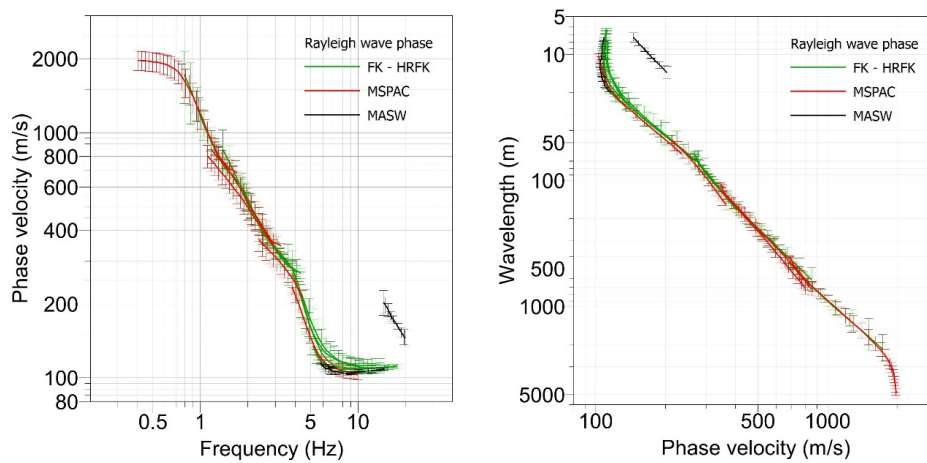

Figure A11.9:   (left) Dispersion curves with Rayleigh wave phase velocity as a function of frequency extracted with the various methods by using FK-based (green dots), MSPAC (red dots), and MASW (black dots) (right) Same dispersion curves represented with wavelength as a function of phase velocity.
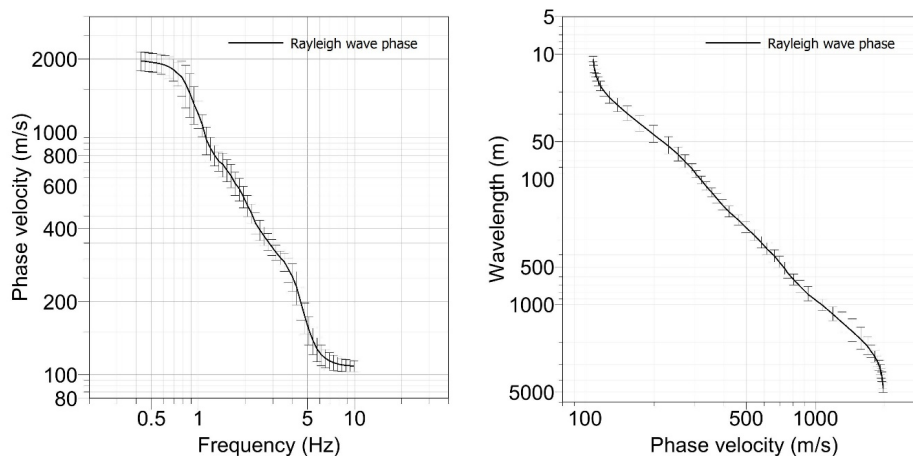

Figure A11.10:   Broad-band dispersion curves considered for the inversion, represented with phase velocity as a function of frequency (left panel) and wavelength in function of phase velocity (right panel))

4.4.2.Inversion strategy

In this section, the strategies adopted for inversion and the type of inversion approach adopted (local search or global search) should be given.

The ground model parameterization consists of 5 uniform layers overlaying a homogeneous half-space. The Poisson's ratio is ranging from 0.2 to 0.5 for all layers in order to limit in an acceptable range the ratio between the compression (V_P) and the shear wave (V_S) velocities. The density of the layers is fixed to 2000 kg/m3. Parameterization for the V_S profile is indicated in Table A11.7 allowing the possibility of a low velocity zone between 20 – 35 m depth, based on geological logs. V_P profiles consists of 5 uniform layers overlaying a homogeneous half-space too, with layer depths linked to V_S profile layers depths and a possibility of low velocity zone between 20 – 35 m. V_P values were allowed to vary between 200 and 5000 m/s.

Table A11.7: Dispersion curve inversion parameterization

Wavelength range used for the dispersion curve inversion (m)	Range of bottom depth (m)	Range of V_S (m/s)	Velocity law
10 - 4903	3 - 8	50 – 300	uniform
	3 - 30	100 – 3500	uniform
	20 - 35	50 - 500	Uniform, low velocity zone allowed
	30 - 700	100 - 3500	uniform
	30 - 2450	150 - 3500	uniform
	Half-space	150 - 3500	uniform

4.4.3.Inversion results

Inversion results are shown in Figure A11.11. Figure A11.11a displays the best shear-wave velocity profile (red line) as well as the ensemble of shear-wave velocity profiles (out of 200400 models) that explain the data within their uncertainty bound ("acceptable solution" concept by Lomax and Snieder, 1994, Souriau et al., 2011).Theoretical dispersion curves obtained from this ensemble of ground models are shown in Figure A11.10b together with the observed phase velocities.
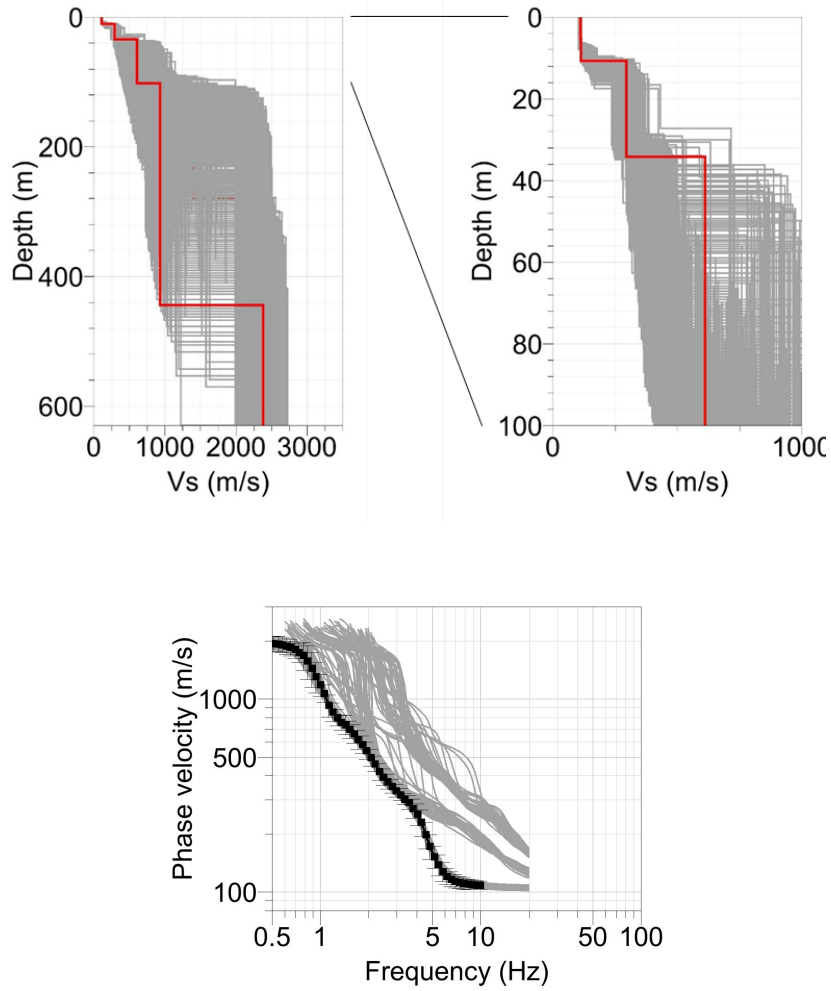
Figure A11.11:   *(top) V_S profiles explaining the observed dispersion data within their uncertainty bound (gray), the red line shows the best misfit V_S profile; (bottom) theoretical dispersion curves computed from the ensemble of inverted shear-wave velocity profiles. The black dots indicate measured phase velocities..*

The best model is a six-layer model that is described in Table A11.8.

Table A11.8: Best model

Layer	Bottom depth	Thickness	Shear-wave Velocity
1	5.2 m	5.2 m	112 m/s
2	10.6 m	5.4 m	114 m/s
3	34.1 m	23.5 m	297 m/s
4	102 m	68 m	612 m/s
5	444 m	342 m	936 m/s
6	-	-	2380 m/s

5. CONCLUSIONS

In this section, the main conclusions of the work in function of the proposed objectives should be given.

Passive and active surface wave data were recorded in the close vicinity of the OGBL station, leading to the determination of the fundamental Rayleigh wave dispersion curve on a wide frequency range (0.5 – 10 Hz).

The inversion of this dispersion curves lead to the estimation of the V_S profile down to about 2000 m depth, showing a velocity increase from 100 m/s in the first 10 m, to 300 – 400 m/s at about 20 – 30 m depth, and a bedrock velocity below 600 m between 2000 and 3000 m/s.

The uncertainties associated to the final result are represented by the set of equivalent shear wave velocity profiles reported in conjunction with the best fitting model. Taking into account the problem of solution non-uniqueness, only the top 40m appears to be characterized with a certain degree of confidence.